Chemical Science

ROYAL SOCIETY OF CHEMISTRY

EDGE ARTICLE

View Article Online
View Journal

Cite this: DOI: 10.1039/d5sc09412g

All publication charges for this article have been paid for by the Royal Society of Chemistry

A secondary-sphere proton channel accelerating metal–hydride formation in Mn(I) catalysts for selective CO_2-to-formate conversion

Min-Jong Bong, †[ab] Wonjung Lee, †[cd] Daehan Lee,[a] Hyunuk Kim,[ab] Junhyeok Seo *[cd] and Ho-Jin Son *[ab]

The selective formation of metal–hydride intermediates represents a key mechanistic step in Mn-based CO_2 reduction catalysis, yet remains kinetically challenging. Herein, we report the discovery of a secondary-sphere proton channel that markedly accelerates Mn–H formation in visible-light-driven CO_2-to-formate conversion. Mn(I) bipyridyl complexes bearing ethylene-bridged Brønsted acidic and basic pendants at the 6,6′-positions of the ligand establish a dynamic hydrogen-bond network that relays protons from protonated triethanolamine (TEOA(H)) directly to the metal center. *Operando* FTIR and DFT analyses reveal that this bio-inspired secondary coordination sphere (SCS) mimics the proton-transfer architecture of formate dehydrogenase (FDH), lowering the activation barrier for hydride formation while suppressing Mn–Mn dimerization. The optimized **Mn-bpy^{diOMe}** complex achieves a turnover number (TON) of approximately 300 and an exceptional formate selectivity exceeding 94%, representing the highest reported among Mn-based molecular systems to date. These findings demonstrate that strategic SCS engineering can emulate enzymatic proton channels, enabling precise control over hydride chemistry and guiding Mn-catalyzed CO_2 reduction exclusively toward formate formation.

Received 2nd December 2025
Accepted 9th March 2026

DOI: 10.1039/d5sc09412g

rsc.li/chemical-science

Introduction

Because of escalating rates of fossil fuel combustion, carbon dioxide (CO_2) emissions have led to environmental issues like climate change and ocean acidification in recent years. These issues have not only impacted the environment but also had socio-economic consequences, underscoring the urgency of achieving carbon neutrality. Consequently, there has been a global focus on the advancement of carbon capture, utilization, and storage (CCUS) technologies.[1–3] Research is actively underway to harness carbon dioxide, the cornerstone of CCUS technology, and convert it into valuable C_1 feedstocks (such as CO, formate, CH_3OH, CH_4, *etc.*) utilizing catalysts. Among the diverse strategies, considerable interest lies in CO_2 conversion systems that utilize molecular transition metal complexes (a combination between d-block elements and electron-pair donors) as catalytic sites.[4–8] The primary advantage of molecular catalysts is their ability to efficiently reduce CO_2 through proton-coupled reaction, significantly lowering the large overpotential required for multi-electron processes. The CO_2-to-C_1 conversion efficiencies can be finely regulated by modifying the electronic structure and bulkiness of coordinating ligands, which directly impacts the redox characteristics of the multivalent transition metal.[9–12]

Nature's handling of proton transfer at transition metal centers follows patterns that are fundamentally familiar to synthetic chemists. Electron-rich, low-valent sites are often prone to protonation, forming metal–hydride intermediates that serve as key species in hydrogen evolution and reduction catalysis. Biological hydrogenases offer a paradigmatic example of this principle. In [FeFe]–hydrogenases,[13–16] the azadithiolate (adt^{2-} = –$SCH_2N(H)CH_2S$–) cofactor acts as an internal proton relay, bridging two low-spin Fe centers through sulfur donors (Fig. 1a). The secondary amine within the adt ligand shuttles H^+ toward the Fe center in concert with electron flow from an adjacent $[4Fe–4S]^+$ cluster, functioning as a molecular proton–electron coupling site. This geometric arrangement forms a "frustrated Lewis pair," where the amine (Lewis base) and Fe (Lewis acid) remain spatially separated yet cooperatively mediate concerted proton transfer. Although direct observation of Fe–H ligation remains challenging, transient hydride intermediates are strongly implicated in catalytic turnover.[17] The

[a]*Department of Advanced Materials Chemistry, Korea University, Sejong 30019, Republic of Korea. E-mail: hjson@korea.ac.kr*

[b]*Division of Smart Energy Convergence Engineering, Korea University, Sejong 30019, Republic of Korea*

[c]*Department of Chemistry, Gwangju Institute of Science and Technology (GIST), Gwangju 61005, Republic of Korea. E-mail: seojh@gist.ac.kr*

[d]*Research Center for Innovative Energy and Carbon Optimized Synthesis for Chemicals (Inn-ECOSysChem), Gwangju Institute of Science and Technology (GIST), Gwangju 61005, Republic of Korea*

† These authors contributed equally to this work.

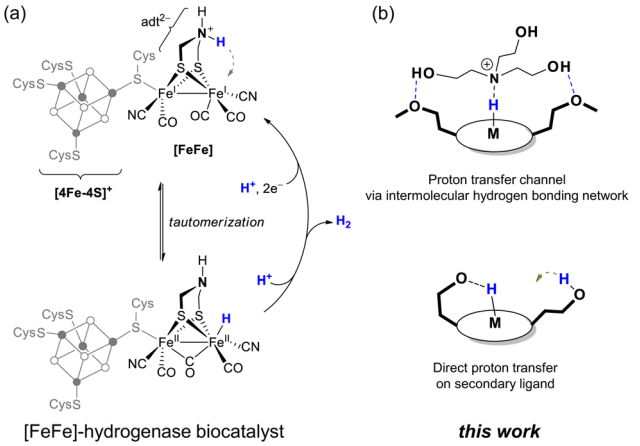

Fig. 1 (a) Simplified structure of the [FeFe]-hydrogenase active site showing proton transfer *via* the azadithiolate (adt^{2-}) bridge, enabling reversible H_2 evolution through a transient Fe–H species. (b) Biomimetic design of secondary-sphere ligands promoting metal–hydride formation through intramolecular or directional proton transfer pathways (this work).

deprotonation of Fe(η^2-H_2) by the secondary amine generates an ammonium–hydride pair, which evolves through PCET to complete the H_2 evolution and oxidation cycles. This architecture exemplifies how secondary coordination enables directional proton relays, stabilizes reactive intermediates, and orchestrates efficient hydride chemistry under mild conditions.

Although numerous secondary coordination sphere (SCS) strategies have been developed to emulate such enzymatic proton channels,[18–22] current approaches remain largely confined to a limited set of ligand architectures, and successful implementations are still scarce. Most reported SCS frameworks fail to achieve the simultaneous control of both proton directionality and metal–hydride selectivity, which is essential for driving CO_2 reduction toward a single desired product. Consequently, there is a pressing need for rationally designed SCS ligands that can selectively promote metal–hydride formation while suppressing side pathways, thereby enabling efficient and selective CO_2-to-formate conversion. From this perspective, effective secondary-sphere regulation remains one of the most challenging and promising frontiers in molecular catalysis. Specifically, Brønsted acidic and basic groups in SCLs are utilized to engage in hydrogen-bonding interactions with bound substrates or directly act as proton relays, facilitating the formation of metal–hydride [M^{2+}–H] (Fig. 1b).[19] It has been established that the optimal choice of transition metal depends on the nature of the ligand, with the SCL effect varying significantly across different systems.[18,23–30]

Recently, first-row transition metals such as Mn(I), Co(II), Fe(II), and Ni(II) have been proposed as viable alternatives to noble metals, which are less practical for large-scale applications due to their high cost and limited availability.[7,12] Among these, mono-bipyridyl Mn(I) complexes have emerged as promising catalysts for electrochemical and photochemical CO_2 reduction, owing to their low cost, environmental compatibility, and efficient catalytic performance.[10,31] However, despite extensive research on Mn(I) catalysts for CO_2 reduction, most reported systems—particularly in electrocatalytic studies—preferentially yield CO rather than formate.[32–37] Although recent efforts involving secondary-sphere modulation or the use of external additives have improved reactivity to some extent, formate selectivity typically remains below 70%, and examples surpassing 90% are exceedingly rare.[38] These limitations highlight the continuing challenge of establishing a robust proton relay that promotes hydride formation and steers Mn catalysis exclusively toward selective CO_2-to-formate conversion.

In this study, we introduce Brønsted acidic and basic secondary coordination ligands (SCLs) at the *ortho*(6)-position of the 4,4′-di-*tert*-butyl-2,2′-bipyridyl ligand, resulting in a series of mononuclear manganese complexes functionalized with ethyl-bridged SCLs: [Mn(I)(6,6′-R_1,R_2-bpy)$(CO)_3$Br] (bpy = 4,4′-di-*tert*-butyl-2,2′-bipyridine). The functionalized Mn(I) complexes include **Mn-bpy^{OH}** (R_1 = –$(CH_2)_2$–OH, R_2 = H), **Mn-bpy^{diOH}** (R_1, R_2 = –$(CH_2)_2$–OH), **Mn-bpy^{OMe}** (R_1 = –$(CH_2)_2$–OMe, R_2 = H), **Mn-bpy^{diOMe}** (R_1, R_2 = –$(CH_2)_2$–OMe), and **Mn-bpy^{OEt}** (R_1 = –$(CH_2)_2$–OEt, R_2 = H) (Fig. 2). In this series, the flexible ethylene linker allows free movement of pendant groups (–OH and –OMe/–OEt), which is expected to facilitate efficient proton transfer to the metal site. This flexibility also helps stabilize key intermediates, such as metal–hydride, through inter- and intramolecular hydrogen bonding between the metal-coordinated species and the Brønsted acidic/basic pendant groups. The catalytic performance of mono-bipyridyl Mn(I) complexes was evaluated in a homogeneous system utilizing a visible-light-responsive heteroleptic Ir(III) photosensitizer, $[Ir(C^N)_2(N^N)]^+$, where C^N represents 1-phenylisoquinoline and N^N denotes 4,4′-dimethyl-2,2′-bipyridine,[39] in combination with the Mn(I) catalyst. Compared to the pristine Mn(I) catalyst without SCLs, the inclusion of Brønsted acidic (–OH) and basic (–OMe and –OEt) SCLs significantly enhanced both catalytic activity and product selectivity. Mechanistic investigations combining *in situ* FTIR spectroscopy and DFT calculations reveal that directional hydrogen bonding between the basic (–OMe) SCLs and protonated TEOA (TEOA(H)) positions the proton in close proximity to the Mn center, thereby substantially reducing the activation barrier for Mn–H formation and promoting the selective generation of formate. Furthermore, the SCLs effectively inhibited the dimerization of the Mn(I) catalyst, which typically compromises durability and favors an undesirable CO_2-to-CO conversion pathway.

Results and discussion

Synthesis and characterization

Scheme 1 shows the synthetic scheme of the Mn(I) complexes having various pendant groups. First, a series of functionalized 6,6′-R_1,R_2-2,2′-bipyridine ligands have been prepared in two or three steps from 4,4′-di-*tert*-butyl-6-methyl-2,2′-bipyridine (**bpy^{Me}**)[40] and 4,4′-di-*tert*-butyl-6,6′-dimethyl-2,2′-bipyridine (**bpy^{diMe}**):[41] LDA/THF-mediated lithiation followed by reaction with paraformaldehyde (for the –$(CH_2)_2$–OH-containing ligand) and reaction with iodoalkyl (alkyl = methane or ethane) after deprotonation by KOH (for the –$(CH_2)_2$–OMe/OEt-containing

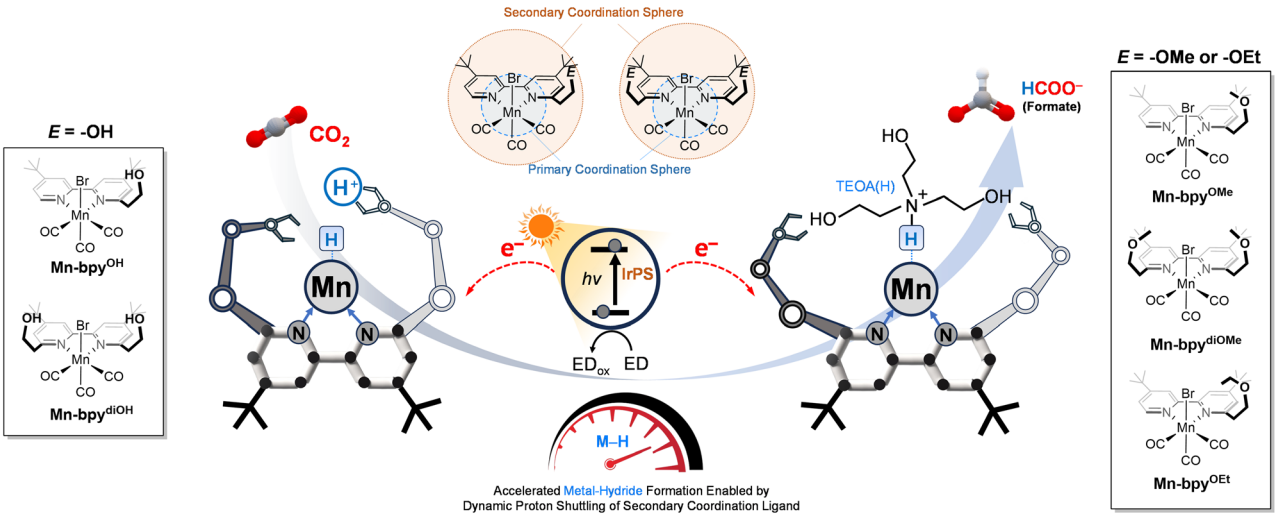

Fig. 2 Schematic illustration of the dye-sensitized Mn(I) system for CO_2 reduction. Photoinduced electron transfer from IrPS promotes Mn–H formation *via* secondary-sphere proton shuttling, enabling efficient CO_2-to-formate conversion under visible light irradiation.

ligand). These ligands include **bpy^{OH}** (R_1 = –$(CH_2)_2$–OH, R_2 = H), **bpy^{OMe}** (R_1 = –$(CH_2)_2$–OMe, R_2 = H), **bpy^{OEt}** (R_1 = –$(CH_2)_2$–OEt, R_2 = H), **bpy^{diOH}** (R_1 = –$(CH_2)_2$–OH, R_2 = –$(CH_2)_2$–OH), and **bpy^{diOMe}** (R_1 = –$(CH_2)_2$–OMe, R_2 = –$(CH_2)_2$–OMe) (see Scheme 1). A series of functionalized Mn(I) complexes (**Mn-bpy^{OH}**, **Mn-bpy^{OMe}**, **Mn-bpy^{OEt}**, **Mn-bpy^{diOH}**, and **Mn-bpy^{diOMe}**) were synthesized by reaction of $Mn(CO)_5Br$ and the functionalized bpy ligands (**bpy^{OH}**, **bpy^{OMe}**, **bpy^{OEt}**, **bpy^{Bu}**, **bpy^{diOH}**, and **bpy^{diOMe}**). (see Scheme 1 and the Experimental section). For comparison, two control samples (**Mn-bpy** and **Mn-bpy^{Bu}**) having no functional group were also prepared by Mn(I) metalation of the parent 4,4′-di-*tert*-butyl–2,2′-bipyridine (bpy) ligand and the butyl-containing bpy ligand (**bpy^{Bu}**). In an effort to build the dark catalysis of Mn(I) catalysts in a photochemical CO_2 reduction system, we also synthesized a lower energy-sensitizing Ir(III) photosensitizer (IrPS), $[Ir(piq)_2(dmb)]^+$ (piq = 1-phenylisoquinoline; dmb = 4,4′-dimethyl-2,2′-bipyridine) according to a previous report.[39] The lower energy photosensitizing capability of IrPS reaching beyond λ > 500 nm prevents the photoexcitation of the Mn(I) catalyst because IrPS can harvest the photoenergy at more than 500 nm that does not overlap with the absorption band of the Mn(I) catalyst. ^{1}H NMR and ESI-mass spectra were used to characterize all Mn(I) complexes (Fig. S3–S26). The structures of **Mn-bpy^{OEt}** and **Mn-bpy^{diOMe}** were confirmed using single-crystal X-ray crystallography (Fig. 3). Both complexes have a facial octahedral geometry

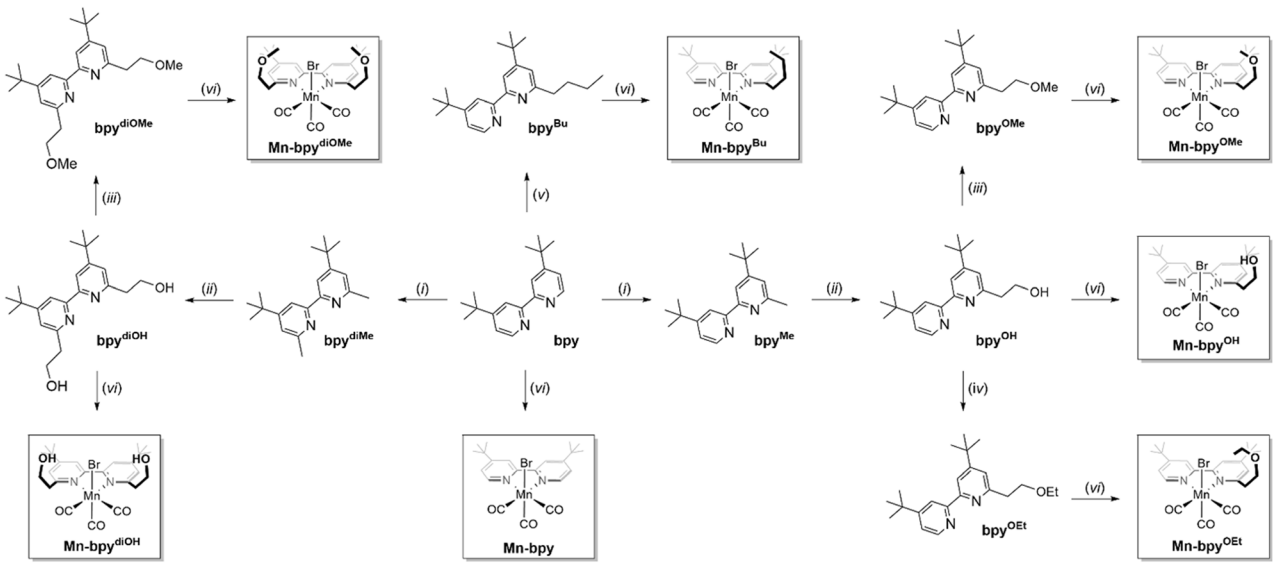

Scheme 1 Synthetic route to mono-bipyridyl Mn(I) complexes under the given conditions: (i) MeLi, diethyl ether, 0 °C, 8 h; (ii) LDA, paraformaldehyde, THF, −78 °C, 10 h; (iii) KOH, iodomethane, ACN, 5 h; (iv) KOH, iodoethane, ACN, 5 h; (v) *n*-BuLi, THF, 0 °C, 10 h; (vi) $[Mn(CO)_5Br]$, diethyl ether, 50 °C, 10 h.

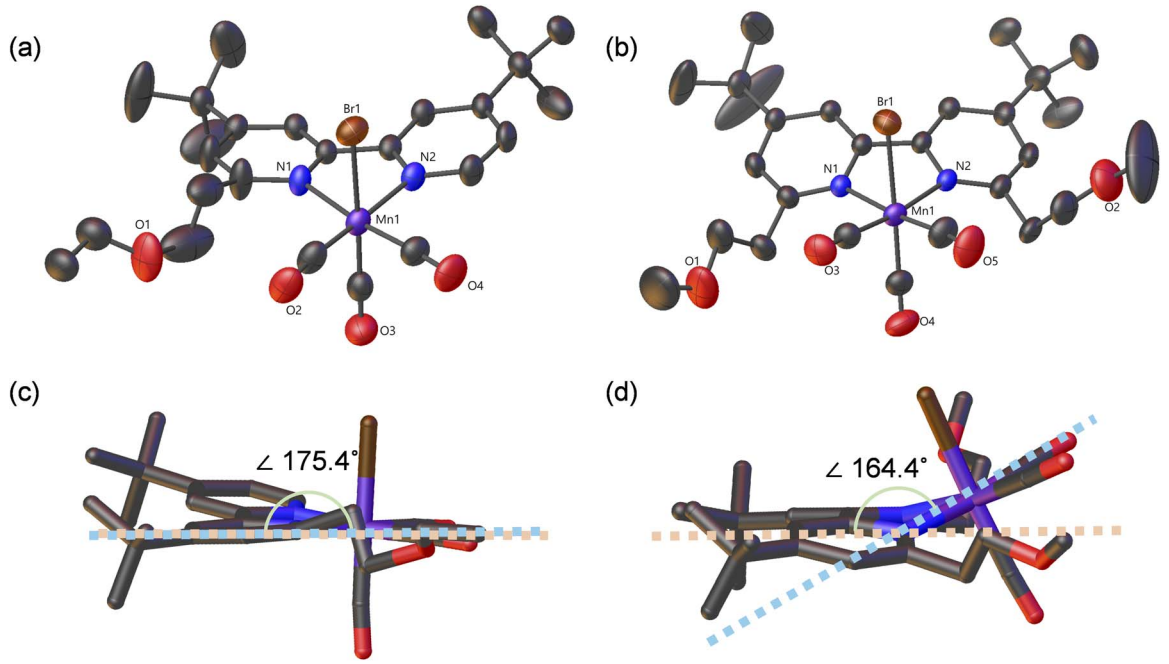

Fig. 3 X-ray crystal structures of (a) **Mn-bpy^{OEt}** and (b) **Mn-bpy^{diOMe}** (30% probability thermal ellipsoids; H atoms omitted). Side views highlight the bpy-Mn torsion angles ((c) $\theta = 175.4°$ for **Mn-bpy^{OEt}** and (d) $\theta = 164.4°$ for **Mn-bpy^{diOMe}**), with dashed lines denoting the reference planes.

around the central Mn atom, with an SCL-tagged bpy ligand and two CO ligands in the equatorial plane, while a bromide group and a third CO ligand occupy axial positions. The solid-state structures show slight distortions from an ideal octahedral shape due to steric effects. Notably, the bipyridine backbone is distorted because of bulky SCL groups at the 6,6′-positions. This distortion is more pronounced in **Mn-bpy^{diOMe}**, which has two ethylene methoxy (–$(CH_2)_2$–OMe) groups, compared to **Mn-bpy^{OEt}** (torsion angles: 175.4° for **Mn-bpy^{OEt}** and 164.4° for **Mn-bpy^{diOMe}**) (see Fig. 3c and d). Additionally, in **Mn-bpy^{diOMe}**, the Mn center is noticeably displaced from the bpy plane, a deviation not observed in **Mn-bpy^{OEt}**. These findings indicate that steric interactions between the SCL groups and the bipyridine ligand significantly alter the facial octahedral environment of the Mn(I) complex.

Photocatalytic activity

The catalytic activity of Mn(I) catalysts was evaluated in an IrPS-sensitized homogeneous system (IrPS + Mn(I) catalyst). All homogeneous samples, prepared in CO_2-saturated DMA or a DMA/additive mixture (additive = 0 to 16.7 vol% triethanolamine (TEOA)) with 0.1 M BIH, were irradiated with low-energy light ($\lambda > 500$ nm) using a 60 W LED lamp (model Fc-6051, Cree Inc.) to assess the catalytic behavior of the Mn(I) catalyst under dark conditions. 1,3-Dimethyl-2-phenyl-1,3-dihydrobenzimidazole (BIH) served as the sacrificial electron donor (SED), ensuring continuous generation of the reductively quenched Ir(III) photosensitizer ($IrPS^{\bullet-}$) throughout the photoreaction. In this homogeneous system, the primary electron transfer mechanism involves collisional electron injection from $IrPS^{\bullet-}$ to the Mn(I) catalyst in solution, as established in previous studies.[7] Tables 1 and 2 summarize the product distributions (formate, CO, and H_2) obtained from all photolysis experiments, providing the net formation of CO_2 reduction products in micromoles and the corresponding turnover numbers (TONs, defined as moles of product per mole of the Mn(I) catalyst).

To optimize the concentrations of the catalyst and IrPS employed in the photoreaction, we systematically adjusted their respective amounts using **Mn-bpy^{diOMe}** as a reference system (Fig. S27). We first tested the conversion activity of the homogeneous system by changing the catalyst concentration from 0.01 to 0.2 mM. As shown in Table 1, the best catalyst concentration in this mixed homogeneous system (IrPS + Mn(I) catalyst) was 0.1 mM. At higher concentrations (>0.1 mM), the high product selectivity for formate suggests that dimer formation, which mainly produces CO, is negligible in the catalysis of **Mn-bpy^{diOMe}** with two bulky –$(CH_2)_2$–OMe groups at the 6,6′-positions of the bpy ligand.[42–44] Subsequently, we assessed the influence of IrPS concentration on reaction activity, varying it from 0.1 mM to 1.0 mM. While the peak catalytic activity was attained at an IrPS loading of 1.0 mM, the enhancement observed upon increasing the concentration from 0.3 mM was only modest. This trend suggests that at 0.3 mM, the system has largely satisfied the requirements for efficient photoinduced electron transfer to the catalyst. Crucially, since the overall turnover is likely rate-limited by catalytic steps slower than the initial reductive quenching, further increments in IrPS loading yield diminishing returns in terms of sensitization efficiency. Consequently, 0.3 mM was identified as the optimal concentration, striking a judicious balance between robust formate production and the efficient utilization of the photosensitizer.

Table 1 Photocatalysis results for the molecular photocatalytic system (IrPS + **Mn-bpy^{diOMe}**) under different conditions[a]

				Formate		CO		
Entry	Catalyst (mM)	IrPS (mM)	$t_{irr.}$ (h)	TON	μmol	TON	μmol	H_2 (μmol)
1	0.2	0.3	3	205 ± 14	123.2 ± 4.1	15 ± 4	8.9 ± 1.1	1.0
2	0.1	0.3	3	296 ± 16	88.7 ± 4.9	18 ± 1	5.5 ± 0.3	0.6
3	0.05	0.3	3	427 ± 6	64.1 ± 1.8	29.5 ± 1	4.4 ± 0.2	0.6
4	0.02	0.3	3	655 ± 8	39.3 ± 2.3	56 ± 1	3.3 ± 0.2	1.3
5	0.01	0.3	3	513 ± 4	15.4 ± 1.1	65	1.9 ± 0.1	0.6
6	0.1	1.0	3	379 ± 11	113.8 ± 3.4	20 ± 3	6.1 ± 0.8	4.3
7	0.1	0.5	3	306 ± 10	91.9 ± 2.9	19 ± 1	5.8 ± 0.4	2.0
8	0.1	0.3	3	296 ± 16	88.7 ± 4.9	18 ± 1	5.5 ± 0.3	0.6
9	0.1	0.1	3	102 ± 9	30.7 ± 2.6	7 ± 1	2.2 ± 0.2	0.3
10[b]	0.1	0.3	3	n.d.[f]	n.d.[f]	n.d.[f]	n.d.[f]	0.6
11[c]	0.1	—	3	n.d.[f]	n.d.[f]	n.d.[f]	n.d.[f]	n.d.[f]
12[d]	0.1	0.3	3	n.d.[f]	n.d.[f]	n.d.[f]	n.d.[f]	n.d.[f]
13[e]	0.1	0.3	3	n.d.[f]	n.d.[f]	n.d.[f]	n.d.[f]	n.d.[f]

[a] Standard photocatalytic conditions: 0.1 M BIH was employed as a sacrificial electron donor in a total solution volume of 3 mL. Reactions were carried out in CO_2-saturated DMA/TEOA (16.7 vol% TEOA) under irradiation with $\lambda > 500$ nm from a 60 W LED lamp (Cree Inc.). [b] Under an Ar atmosphere. [c] In the absence of the Ir(III) photosensitizer (IrPS). [d] Without an electron donor (BIH). [e] In the dark. [f] Not detected.

In the control test, homogeneous photocatalysis without IrPS did not show any CO_2 conversion activity (entry 11 in Table 1). This suggests that both IrPS and the Mn(I) catalyst are necessary for photocatalysis in this system. Additionally, when BIH or light was absent (entries 12 and 13 in Table 1), **Mn-bpy^{diOMe}** showed no catalytic activity. This confirms that CO_2 reduction

Table 2 Additive effects on photocatalytic CO_2 reduction with Mn(I) catalyst-based photocatalytic systems[a]

				Formate		CO				Selectivity[c]%	
Entry	Catalysts	TEOA (vol%)	$t_{irr.}$ (h)	TON	μmol	TON	μmol	H_2 (μmol)	$\Phi_{formate}$ [d](%)	Formate	CO
1	**Mn-bpy**	0	3	4	1.2 ± 0.1	n.d[b]	n.d [b]	n.d.[b]			
2	**Mn-bpy^{OH}**	0	3	11 ± 1	3.4 ± 0.2	n.d[b]	n.d[b]	<0.1			
3	**Mn-bpy^{OMe}**	0	3	12 ± 1	3.6 ± 0.2	n.d[b]	n.d[b]	<0.1			
4	**Mn-bpy^{OEt}**	0	3	12 ± 1	3.6 ± 0.3	n.d[b]	n.d[b]	<0.1			
5	**Mn-bpy^{Bu}**	0	3	4	1.2 ± 0.1	n.d[b]	n.d[b]	n.d.[b]			
6	**Mn-bpy^{diOH}**	0	3	16 ± 1	4.9 ± 0.4	n.d[b]	n.d[b]	<0.1			
7	**Mn-bpy^{diOMe}**	0	3	31 ± 1	9.3 ± 0.3	n.d[b]	n.d[b]	<0.1			
8	**Mn-bpy**	5	3	67 ± 5	20.1 ± 1.6	17 ± 1	5.2 ± 0.2	0.1		79	21
9	**Mn-bpy^{OH}**	5	3	75 ± 7	22.5 ± 2.1	16 ± 1	4.8 ± 0.3	0.3		82	18
10	**Mn-bpy^{OMe}**	5	3	87 ± 4	26.0 ± 1.3	11 ± 1	3.3 ± 0.3	0.2		89	11
11	**Mn-bpy^{OEt}**	5	3	86 ± 6	25.9 ± 1.8	16 ± 1	4.8 ± 0.2	0.3		84	16
12	**Mn-bpy^{Bu}**	5	3	45 ± 3	13.5 ± 0.9	13 ± 1	4.0 ± 0.1	0.1		77	23
13	**Mn-bpy^{diOH}**	5	3	75 ± 4	22.5 ± 1.1	14 ± 1	4.2 ± 0.2	0.1		84	16
14	**Mn-bpy^{diOMe}**	5	3	122 ± 7	36.6 ± 2.1	15	4.6 ± 0.1	0.2		89	11
15	**Mn-bpy**	10	3	76 ± 4	22.9 ± 1.2	33 ± 1	9.8 ± 0.4	0.2		70	30
16	**Mn-bpy^{OH}**	10	3	96 ± 5	28.9 ± 1.6	24 ± 1	7.2 ± 0.2	0.5		80	20
17	**Mn-bpy^{OMe}**	10	3	129 ± 8	38.8 ± 2.4	20 ± 1	5.9 ± 0.2	0.4		87	13
18	**Mn-bpy^{OEt}**	10	3	99 ± 9	29.6 ± 2.8	14.1 ± 1	4.2 ± 0.3	0.4		87	13
19	**Mn-bpy^{Bu}**	10	3	68 ± 5	20.5 ± 1.4	21 ± 2	6.2 ± 0.5	0.4		76	24
20	**Mn-bpy^{diOH}**	10	3	104 ± 4	31.3 ± 1.1	24 ± 1	7.2 ± 0.2	0.3		81	19
21	**Mn-bpy^{diOMe}**	10	3	216 ± 10	64.9 ± 2.9	23	6.8 ± 0.1	0.5		90	10
22	**Mn-bpy**	16.7	3	109 ± 12	32.7 ± 3.6	27 ± 2	8.2 ± 0.7	0.9	5.4	80	20
23	**Mn-bpy^{OH}**	16.7	3	128 ± 9	38.3 ± 2.7	33 ± 1	9.8 ± 0.4	1.2	7.3	80	20
24	**Mn-bpy^{OMe}**	16.7	3	160 ± 11	48.0 ± 3.2	24 ± 1	7.2 ± 0.2	1.1	10.4	87	13
25	**Mn-bpy^{OEt}**	16.7	3	158 ± 12	47.4 ± 3.5	25 ± 2	7.5 ± 0.6	1.1	9.5	86	14
26	**Mn-bpy^{Bu}**	16.7	3	83 ± 8	24.9 ± 2.4	21 ± 1	6.2 ± 0.3	0.9	3.9	80	20
27	**Mn-bpy^{diOH}**	16.7	3	183 ± 11	54.8 ± 3.2	25 ± 1	7.4 ± 0.2	1.2	13.3	88	12
28	**Mn-bpy^{diOMe}**	16.7	3	296 ± 16	88.7 ± 4.9	18 ± 1	5.5 ± 0.3	0.6	25.9	94	6

[a] The following standard conditions were employed: 0.3 mM IrPS, 0.1 mM Mn(I) catalyst, and 0.1 M BIH are commonly used as the photosensitizer, catalyst, and sacrificial electron donor, respectively. The total volume of the solution was 3 mL. All photocatalytic reactions are performed in CO_2-saturated DMA or mixed DMA/TEOA solution (0–16.7 vol% TEOA) at greater than 500 nm emitted from a light emitting diode (LED) lamp (60 W, Cree Inc.). [b] Not detected. [c] Product selectivity percentages represent only the selectivity observed between formate and CO. Hydrogen is also observed to be a minor product in all photoreactions. [d] See the detailed method for QY measurement in the Experimental section.

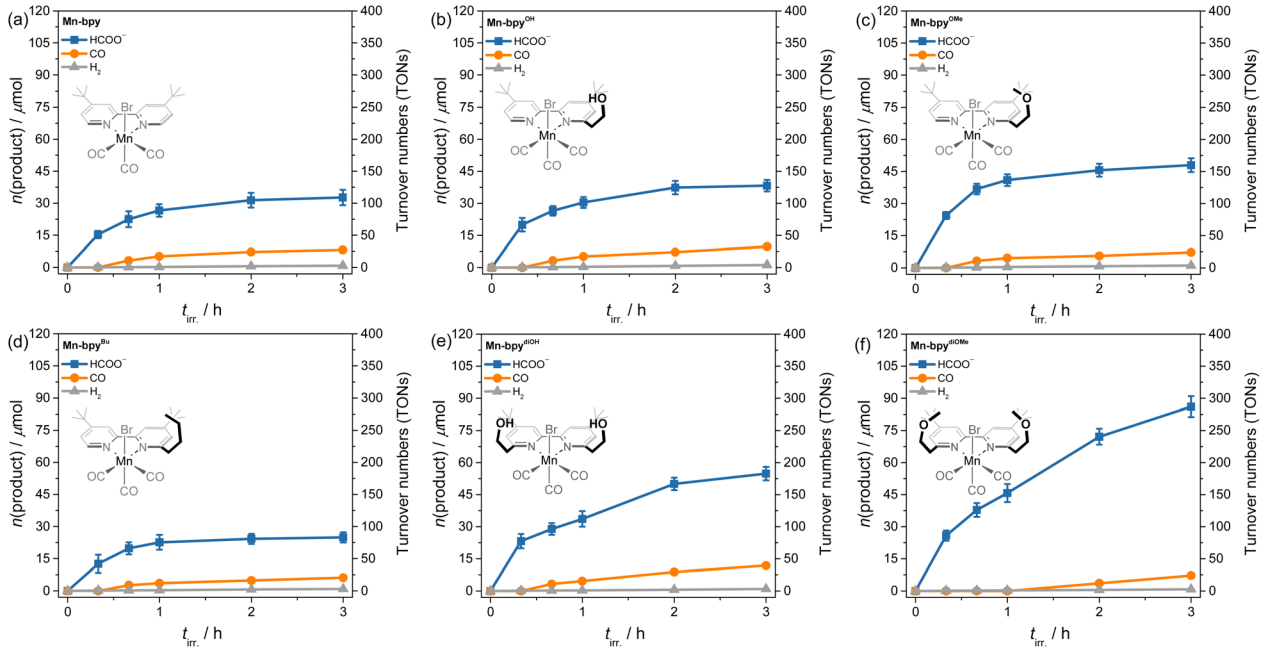

Fig. 4 Plots of formate and CO formation *versus* irradiation time (0 to 3 h) for the homogeneous system [IrPS (0.3 mM) + Mn(I) catalysts (0.1 mM)] (Mn(I) catalyst = (a) **Mn-bpy**, (b) **Mn-bpy^{OH}**, (c) **Mn-bpy^{OMe}**, (d) **Mn-bpy^{Bu}**, (e) **Mn-bpy^{diOH}**, or (f) **Mn-bpy^{diOMe}**) in CO_2-saturated DMA/TEOA (16.7 vol% TEOA) containing 0.1 M BIH; irradiation at $\lambda > 500$ nm.

by the Mn(I) catalyst starts with a photochemical electron transfer from IrPS$^{\bullet-}$ to the Mn(I) catalyst occurring after the IrPS component absorbs light (IrPS + $h\nu$ → IrPS*) and undergoes reductive quenching by the BIH electron donor (IrPS* + BIH → IrPS$^{\bullet-}$ + BIH$^{\bullet+}$). To further investigate the proton-shuttling capability of the tethered functional groups in the catalytic system, we conducted photoreactions using Mn(I) catalysts sensitized with IrPS in the presence of varying concentrations of the TEOA proton donor (0–16.7 vol%) (Table 2 and Fig. S28–S31).

As summarized in Table 2, increasing the concentration of TEOA led to a marked enhancement in both the net formate yield (μmol) and product selectivity for the functionalized Mn(I) catalysts, in sharp contrast to the minimal response observed for the parent **Mn-bpy** complex (Fig. S32). This pronounced dependence on TEOA clearly implicates a critical role of the

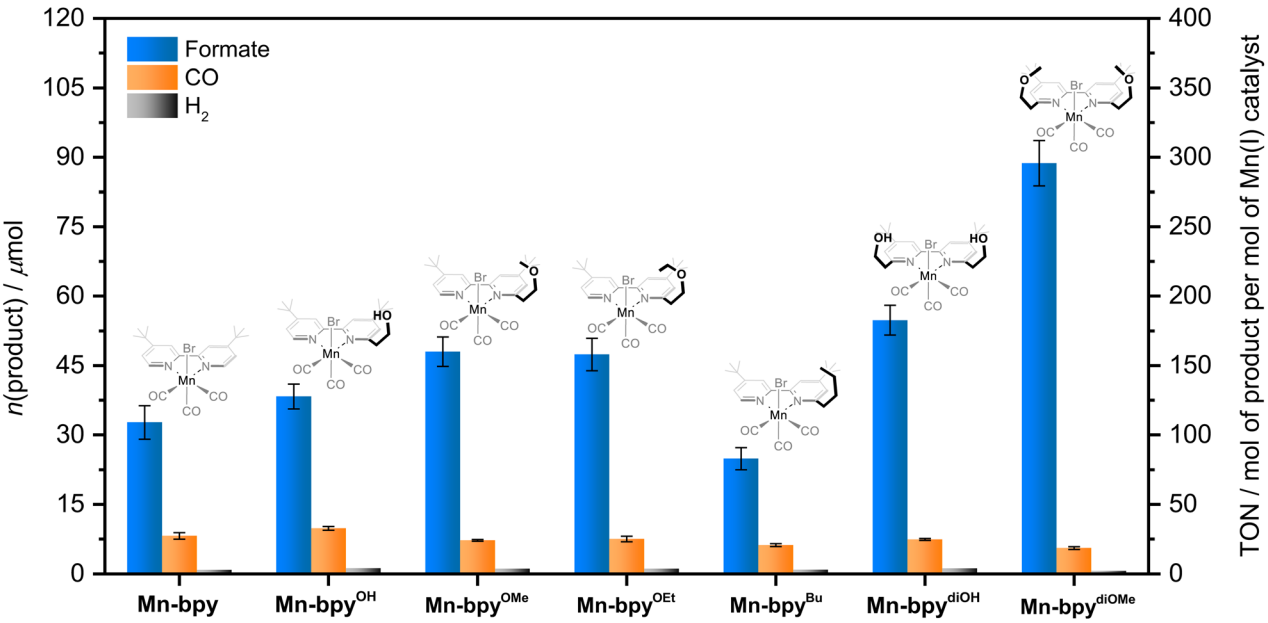

Fig. 5 Photocatalytic CO_2 reduction profiles over 3 h of irradiation ($\lambda > 500$ nm). Homogeneous system: 0.1 mM Mn(I) catalyst, 0.3 mM IrPS, 0.1 M BIH in CO_2-saturated DMA/TEOA solution (16.7 vol% TEOA) at 298 K.

proton donor in modulating catalytic activity. Notably, such enhancement was not observed upon the addition of alternative proton sources such as H_2O, TFE, and PhOH. While a slight increase in formate production was observed with 1.51 M PhOH (4.6 μmol for **Mn-bpy**, 7.9 μmol for **Mn-bpy^{diOH}**, and 16.4 μmol for **Mn-bpy^{diOMe}**), the difference remained marginal, and the overall catalytic performances of all three Mn(I) complexes were similarly low under these conditions (Fig. S33). These results underscore a unique secondary coordination effect operative only in the presence of TEOA, wherein specific intermolecular interactions between the SCLs and TEOA likely facilitate directional proton delivery to the reduced Mn center, thereby promoting CO_2-to-formate conversion.

Isotope-labeling experiments using $^{13}CO_2$ gas were performed to verify that the detected formate ($HCOO^-$, the deprotonated form of formic acid) originated from CO_2 reduction. In this photocatalytic system, direct identification by NMR spectroscopy was not feasible, likely due to the paramagnetic nature of the Mn species. Instead, the protonated formate (HCOOH) was extracted from the reaction mixture using ethyl acetate and aqueous H_2SO_4 and subsequently analyzed by GC-MS (Fig. S34). Under a $^{12}CO_2$ atmosphere, the chromatogram at 6.2 min retention time displayed mass signals at $m/z = 44$, 45, and 46, consistent with an authentic $H^{12}COOH$ reference (Fig. S34a and S34b). When the reaction was carried out under a $^{13}CO_2$ atmosphere, the corresponding peak exhibited a +1 m/z shift, with signals at $m/z = 45$, 46, and 47, attributable to $H^{13}COOH$ (Fig. S34c). These results clearly demonstrate that the detected formate is produced predominantly *via* CO_2 reduction.

As illustrated in Fig. 4 and 5, under proton-rich conditions (16.7 vol% TEOA), the TONs and selectivity of **Mn-bpy^{diOH}** and **Mn-bpy^{diOMe}** exhibit clear enhancements over their monofunctionalized counterparts, demonstrating that the dual-SCL architecture more effectively facilitates proton-coupled electron transfer when proton donors are sufficiently available. Under photocatalytic conditions with an excess of TEOA (16.7 vol%), **Mn-bpy^{diOMe}** demonstrated the highest CO_2-to-formate conversion efficiency, achieving a TON of approximately 300 and a formate yield of 89 μmol. This represents an approximately 2.7-fold increase in catalytic performance relative to the non-functionalized **Mn-bpy**, with formate selectivity reaching ~94%. These findings align with a previous report,[23] which indicates that incorporating two *N*-benzyl-*N*-ethylethanamine tethering groups at the 6,6′-positions of bipyridine, rather than a single substitution, substantially enhances formate selectivity and more than doubles the turnover frequency (TOF). Moreover, the bi-tethered Mn(I) catalysts (**Mn-bpy^{diOMe}** and **Mn-bpy^{diOH}**) exhibited superior long-term catalytic performance (up to 3 h) compared to non-functionalized **Mn-bpy** and mono-tethered Mn(I) catalysts (**Mn-bpy^{OH}**, **Mn-bpy^{OMe}**, and **Mn-bpy^{OEt}**), which commonly displayed early deactivation within 1 h of photolysis. These results underscore the beneficial role of SCLs in enhancing both the efficiency and durability of Mn(I) catalysts. The observed improvements can be attributed to (1) a proton shuttling effect of SCLs, which facilitates H^+ delivery to the reduced metal center, directly promoting metal–hydride intermediate formation and (2) a steric bulk effect of SCLs, which mitigates catalyst deactivation by suppressing dimerization pathways that otherwise limit activity and stability (*vide infra*). In contrast, **Mn-bpy^{Bu}**, synthesized for comparison, exhibited reduced catalytic activity and formate selectivity relative to **Mn-bpy**, further confirming the critical role of Brønsted acidic/basic functionalities in the secondary coordination sphere. Under the optimized conditions (16.7 vol% TEOA), the quantum yields ($\Phi_{formate}$) for formate formation measured at 500 nm across the Mn(I) complexes were found to range from 5.4 to 25.9% (entries 22–28 in Table 2 and Fig. S35).

Electrochemistry

Electrochemical characterization was performed to evaluate how the SCL influences the electrocatalytic properties of Mn(I) complexes. Cyclic voltammetry (CV) measurements were conducted for all Mn(I) complexes in dry DMF with 0.1 M tetrabutylammonium perchlorate (TBAP) as the supporting electrolyte under an Ar atmosphere. In the negative scan direction, SCL-tagged Mn(I) catalysts exhibit two reduction waves at 1.75 V and −2.90 V (*vs.* Fc^+/Fc), corresponding to a slightly less reversible peak and a quasi-reversible peak, respectively. For comparison, the CV of **Mn-bpy** was also recorded under similar conditions. The first reduction wave, with a peak-to-peak separation of ~370 mV, suggests a two-electron process of Mn(I) catalysts, likely accompanied by Br^- loss to generate an anionic species.[44] The reduction peak near −2.9 V is attributed to a bpy ligand-based reduction.[44] In contrast to **Mn-bpy** and the monofunctionalized Mn(I) complexes, which display a prominent anodic peak at approximately −0.54 V (*vs.* Fc^+/Fc)., the difunctionalized catalysts (**Mn-bpy^{diOH}** and **Mn-bpy^{diOMe}**) exhibit a substantially reduced anodic response under Ar. Notably, this feature becomes negligible under catalytic conditions in the presence of TEOA (Fig. 6), supporting the hypothesis that 6,6′-difunctionalization provides sufficient steric or electronic inhibition to effectively suppress dimerization during catalysis.[44] Further CV analysis of **Mn-bpy^{diOH}** and **Mn-bpy^{diOMe}** confirms the absence of a dimerization process (Fig. S36). As shown in our photolysis results, the major product is formate, with a small amount of CO. This indicates that the primary catalytic pathway for CO_2 conversion is the formation of formate *via* a metal–hydride intermediate. To confirm the reduction wave of the metal–hydride species, CV measurements were conducted with 2 mM to 0.1 M H_2SO_4 under an Ar atmosphere. The potential of the metal–hydride intermediate was identified by tracking the emergence of a new reduction wave as the H_2SO_4 concentration increased. This analysis revealed that the reduction wave at ~−2.13 V corresponds to the redox peak of [Mn(I)–hydride]$^{0/-1}$.

To further investigate the electrochemical behavior of Mn(I) complexes and identify key catalytic intermediates under realistic conditions for proton-coupled CO_2 reduction, CV measurements were conducted in a mixed DMF/TEOA solvent system (16.7 vol% TEOA) under an Ar or CO_2 atmosphere. Under an Ar atmosphere with 16.7 vol% TEOA, Mn(I) complexes (**Mn-bpy^{diOH}** and **Mn-bpy^{diOMe}**), which contain two SCLs, exhibited a distinct rise in the reduction wave at ~–2.13 V,

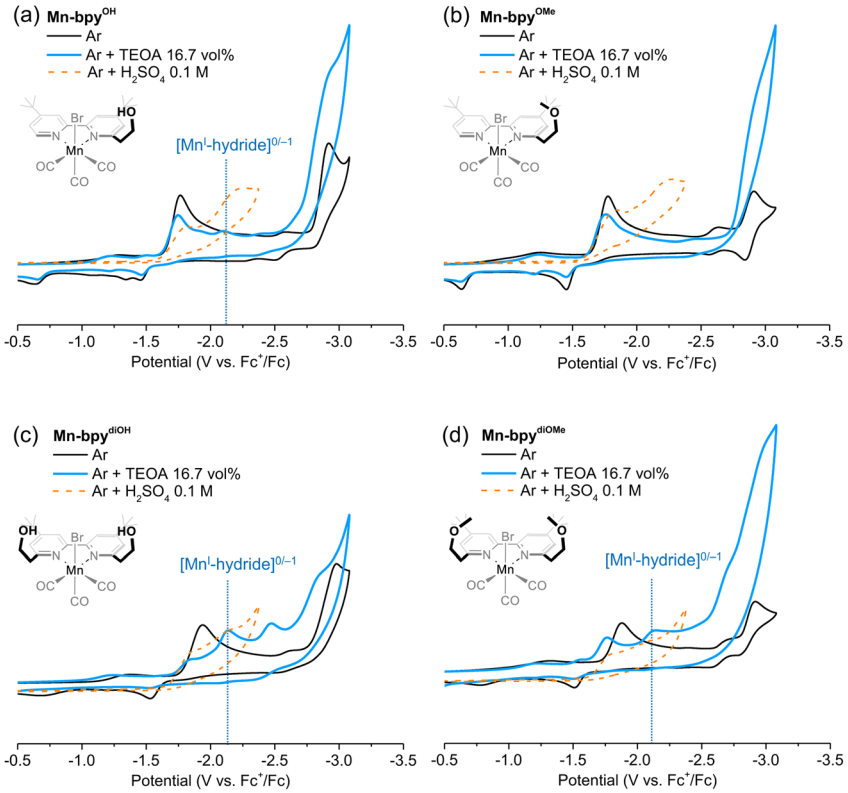

Fig. 6 Cyclic voltammograms of Mn(I) catalysts ((a) **Mn-bpy^{OH}**, (b) **Mn-bpy^{OMe}**, (c) **Mn-bpy^{diOH}**, and (d) **Mn-bpy^{diOMe}**) (1 mM) in Ar-saturated DMF or DMF with additives (16.7 vol% TEOA or 0.1 M H_2SO_4) containing 0.1 M TBAP.

corresponding to the [Mn(I)–hydride]$^{0/-1}$ peak. Simultaneously, the anodic peak near −1.50 V (*vs.* Fc^{+}/Fc) disappeared, and the original reduction peak at around −1.90 V decreased, confirming the formation of the Mn–hydride intermediate through protonation of the two-electron-reduced [(L)Mn^{0}(CO)$_3$]$^{-}$ species (L = 2,2′-bipyridine derivatives). Compared to Mn(I) complexes with only one SCL, the cyclic voltammograms of **Mn-bpy^{diOH}** and **Mn-bpy^{diOMe}** displayed a more pronounced Mn–hydride peak, indicating that the presence of two SCLs significantly enhances proton delivery to the Mn metal center.

This observation is consistent with the superior catalytic performance of these systems in CO_2 reduction compared to Mn(I) complexes bearing a single secondary coordination ligand (SCL). Notably, among **Mn-bpy^{diOH}** and **Mn-bpy^{diOMe}**, the more pronounced increase in the Mn–hydride peak observed in the cyclic voltammograms (CVs) of **Mn-bpy^{diOMe}** correlates with its markedly enhanced CO_2-to-formate conversion efficiency (Fig. 7 and Table 2). On the other hand, at low concentrations of TEOA (5 vol%), the significant rise in the metal–hydride reduction peak for **Mn-bpy^{diOMe}** suggests a strong intermolecular hydrogen-bonding interaction between the pendant –OMe groups and the –OH moieties of the TEOA additive (Fig. 6b). This interaction is proposed to facilitate a proton relay mechanism, positioning the acidic proton of TEOA(H) in close proximity to the nucleophilic Mn center, thereby accelerating hydride formation and enhancing overall catalytic efficiency.

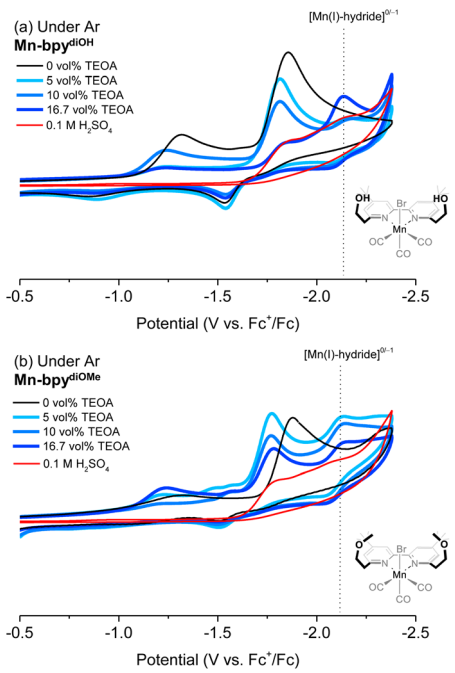

Fig. 7 Cyclic voltammograms of (a) **Mn-bpy^{diOH}** and (b) **Mn-bpy^{diOMe}** in Ar-saturated mixed DMF/TEOA solvent (TEOA = 0 to 16.7 vol%). As the TEOA concentration increases, the linear increase in the redox peak at −2.13 V indicates the increasing amount of the Mn(I)–hydride intermediate.

When both a proton donor and CO_2 gas were present, all Mn(I) complexes exhibited a significant rise in multiple reduction waves between −2.0 and −2.7 V (Fig. S36 and S37). This pronounced increase suggests that CO_2 molecules interact with the Mn–hydride intermediate, forming a metal–formate species. This intermediate subsequently releases formate upon further one-electron reduction. The emergence of more negative cathodic waves confirms the completion of the monomeric CO_2 conversion cycle, regenerating the one-electron-reduced species, $[(L)Mn^0(CO)_3]^-$, which serves as the starting point for the next catalytic cycle. In the absence of both CO_2 gas and the TEOA additive, cathodic peaks between −2.0 and −2.9 V were nearly absent, demonstrating that the coexistence of TEOA and CO_2 is essential for efficient CO_2-to-formate conversion by the mono-bipyridyl Mn(I) catalysts.

In situ FTIR spectrochemical characterization

To gain insight into the enhanced activity and formate selectivity of the SCL-tagged Mn(I) catalyst compared to the pristine **Mn-bpy** catalyst and to elucidate the underlying catalytic mechanism, a comparative FTIR analysis was conducted under conditions closely resembling actual photolysis conditions. This analysis employed a custom-built *operando* FTIR spectrochemical setup for a mixed homogeneous system. A CO_2-saturated DMA/additive solution (5 vol% TEOA) containing bipyridyl Mn(I) catalysts (1 mM), IrPS (1 mM), and BIH (0.1 M) was introduced into an IR-beam-transmitting active cell with a CaF_2 window (Fig. S2). The FTIR spectra of all Mn(I) catalysts were then compared with literature-reported values (Fig. S38–S44).[23,45,46] Before irradiation, the IR peak value of the pristine 4,4′-di-*tert*-butyl-substituted **Mn-bpy** complex closely matches the literature values.[45] For the SCL-tagged Mn(I) catalyst, the mono-tethered and di-tethered Mn(I) complexes exhibited IR peak shifts to lower frequencies by 2 cm^{-1} and 4 cm^{-1}, respectively (2020, 1929, and 1909 cm^{-1} for **Mn-bpy**; 2018–2017, 1925–1922, and 1910–1909 cm^{-1} for one SCL-tethered Mn(I) catalysts; 2017–2016, 1925, and 1908 cm^{-1} for two SCL-tethered Mn(I) catalysts). This shift is attributed to an enhanced back-bonding effect from the bpy ligand to the Mn center due to the incorporation of a functionalized ethylene group.

Fig. 8 illustrates the evolution of FTIR bands in an Mn(I) complex with three CO ligands under irradiation (λ > 495 nm) for 0–180 minutes. This analysis offers crucial insights into the catalytic mechanism by tracking changes in electron density on the Mn center. A general decrease in the 2050–1850 cm^{-1} spectral region suggests a transformation of the Mn(I) catalyst upon photochemical reduction, though substantial peak overlap makes it challenging to distinguish individual Mn(I) species. As expected, the **Mn-bpy** catalyst without the SCL ligand showed a noticeable peak at around 1968 cm^{-1}, which corresponds to the Mn–Mn dimer. Previous research by Grills *et al.* showed that reduction of $[(L)Mn(CO)_3X]$ produces a radical species, $[(L)Mn^I(CO)_3]^\bullet$, in which much of the spin density is localized on the Mn center (ρ_a = 0.47), thereby favoring Mn–Mn dimer formation.[10] In contrast, the analogous Re(I) radical ($[(L)Re^I(CO)_3]^\bullet$) displays a lower metal-centered spin density (ρ_a = 0.25) due to pronounced delocalization between the Re center and the bpy ligand, which suppresses dimerization.[10] Interestingly, the SCL-tethered Mn(I) catalysts did not exhibit any Mn–Mn dimer peaks. This absence indicates that the alkyl tethering groups impose sufficient steric hindrance to block Mn–Mn

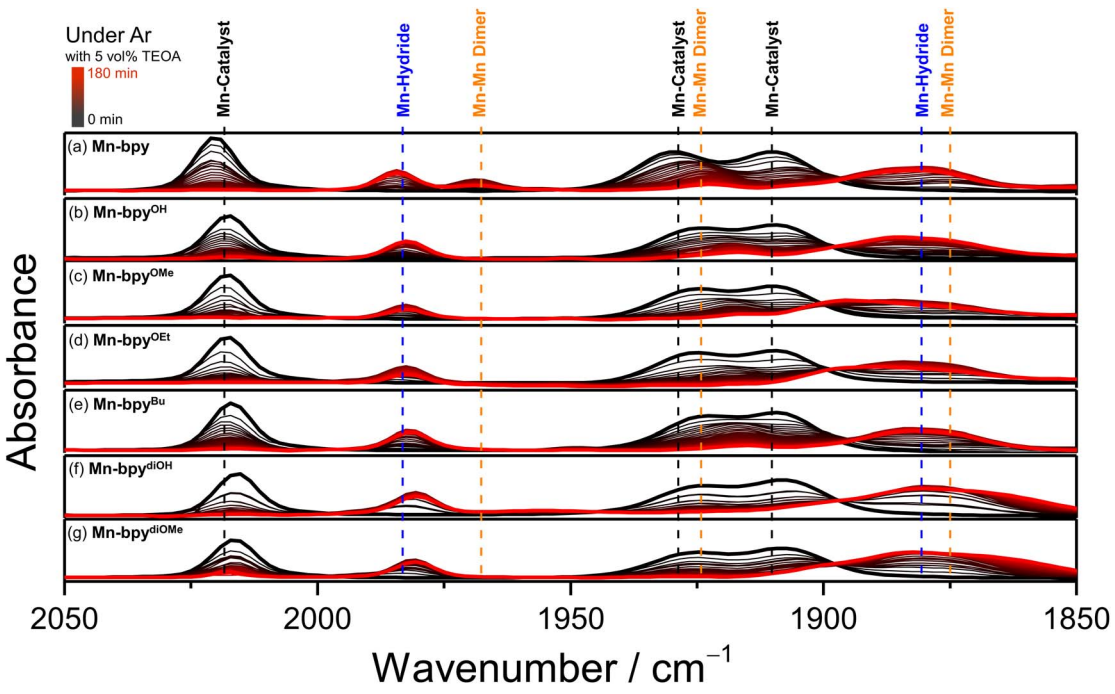

Fig. 8 FTIR spectral changes following irradiation time for the 1 mM IrPS + 1 mM Mn(I) catalyst in 0.03 mL of Ar-saturated DMA/TEOA solution (5 vol% TEOA) containing 0.1 M BIH.

interactions, thereby stabilizing the monomeric pathway and enabling more sustained and controlled catalytic activity.

Under an Ar atmosphere with TEOA, prolonged irradiation led to a notable increase in the CO vibration peak within the 1987–1870 cm^{-1} region for all Mn(I) complexes, indicating the formation of a Mn–hydride intermediate *via* protonation of the reduced Mn(I) complex during the photoreaction. A comparison of Mn–hydride formation rates under Ar conditions, as shown in Fig. 9, revealed clear differences among the Mn(I) complexes. The **Mn-bpy** catalyst possessing no SCL required approximately 70 minutes to complete Mn–hydride formation, whereas the SCL-tethered Mn(I) catalysts formed Mn–hydrides within 25 minutes. These results suggest that the SCL groups help form the Mn–hydride intermediate. In the case of **Mn-bpy^{Bu}** having no secondary functional group, the formation of Mn–hydride was completed in about 30 minutes, faster than that of pristine **Mn-bpy**. This phenomenon is attributed to the suppression of dimerization during the early activation, caused by the steric hindrance of the tethered butyl group. In other words, the reduced probability of dimerization in the **Mn-bpy^{Bu}** catalyst appears to accelerate the Mn–hydride formation rate. Notably, **Mn-bpy^{diOMe}** and **Mn-bpy^{diOH}**, which contain two SCL groups at the 6,6′-positions of the bpy ligand, exhibited an even faster Mn–hydride formation rate (less than 15 minutes) compared to mono-SCL-tethered Mn(I) catalysts.

This suggests that as the number of SCLs increases, the chance of proton shuttling also increases, leading to a faster formation rate of the metal–hydride intermediate. This result is consistent with the electrochemical findings for **Mn-bpy^{diOH}** and **Mn-bpy^{diOMe}**, which show a distinct [Mn^{I}–hydride]$^{0/-1}$ peak at around −2.13 V, unlike other Mn(I) complexes that exhibit a lower peak or lack it entirely (Fig. 6 and S37d). It should be also noted that **Mn-bpy^{OH}** and **Mn-bpy^{diOH}** containing the –$(CH_2)_2$–OH group showed a faster Mn–hydride formation rate than other Mn(I) complexes possessing –$(CH_2)_2$–OMe or –$(CH_2)_2$–OEt group as SCLs. This is attributed to the presence of a hydroxyl group (–OH), which has a lower pK_a value than TEOA, enabling direct intramolecular hydrogen transfer within the catalyst and thereby accelerating the proton shuttling rate.[47] This hypothesis is well supported by the electrochemical behavior of **Mn-bpy^{OH}** and **Mn-bpy^{diOH}** showing a discernible rise of the [Mn^{I}–hydride]$^{0/-1}$ peak upon the addition of TEOA as a proton source (Fig. 6a and c).

Fig. S45 presents the FTIR spectral evolution of CO vibration peaks upon irradiation in CO_2-saturated DMA/TEOA (5 vol% TEOA). Compared to the Ar atmosphere with TEOA, the introduction of CO_2 gas led to a rapid decrease in the Mn–hydride peak at 1987–1870 cm^{-1}, accompanied by the emergence of multiple peaks at lower wavenumbers (1920–1850 cm^{-1}). This spectral evolution indicates that the generated Mn–H species is subsequently consumed through catalytic steps involving the formation of Mn–formate *via* its reaction with CO_2, followed by the release of formate from the Mn–formate intermediate. Notably, for all Mn(I) catalysts, no distinct increase was observed in the CO vibration region of 2004–2000 cm^{-1}, which corresponds to the Mn–formate species. This result contrasts sharply with our previous result, where ethylene-bridged SCLs (–$(CH_2)_2$–OH and –$(CH_2)_2$–NMe_2 groups) excessively stabilized the Ru(I)–formate intermediate, leading to its gradual accumulation over time during photoreaction.[47] The absence of a detectable Mn–formate peak suggests that formate readily dissociates from the Mn(I)–formate species. This, in turn, may

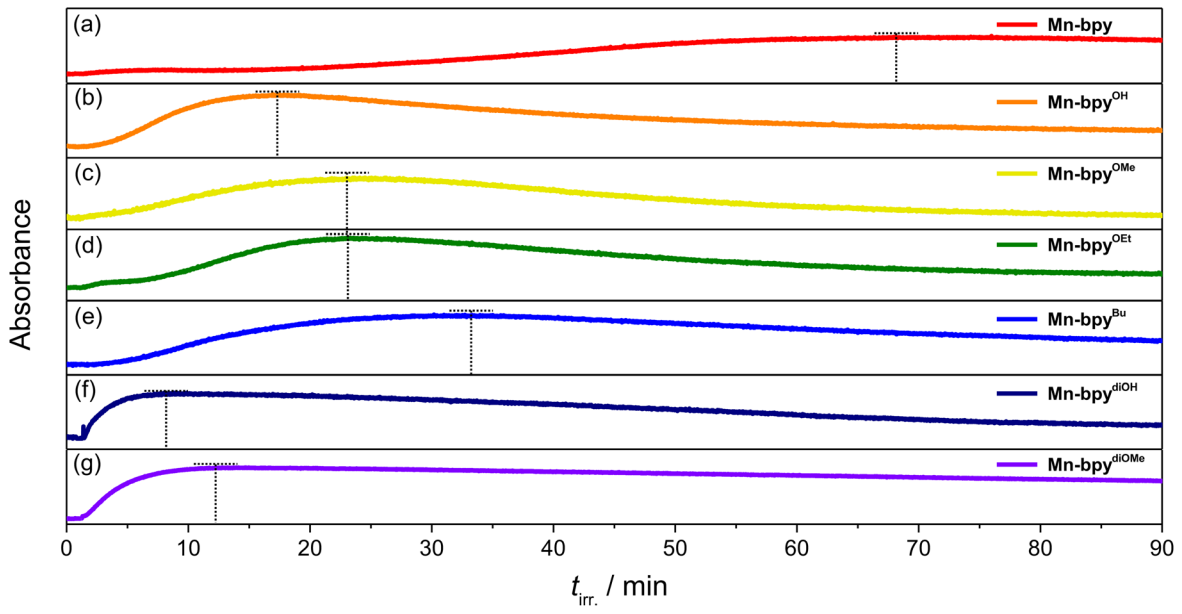

Fig. 9 Time-resolved FTIR spectral evolution at 1983 cm^{-1} during 1.5 h of photolysis for a solution containing 1 mM IrPS and 1 mM Mn(I) catalyst ((a) **Mn-bpy**, (b) **Mn-bpy^{OH}**, (c) **Mn-bpy^{OMe}**, (d) **Mn-bpy^{OEt}**, (e) **Mn-bpy^{Bu}**, (f) **Mn-bpy^{diOH}**, and (g) **Mn-bpy^{diOMe}**) in 0.03 mL of Ar-saturated DMA/TEOA (5 vol%) with 0.1 M BIH. The growth of the 1980–1984 cm^{-1} absorption band reflects the time-dependent formation of Mn–hydride intermediates.

explain the higher CO_2-to-formate conversion activities of Mn(I) complexes compared to mono-bipyridyl Ru(II) complexes. Meanwhile, the more intense Mn–hydride peak observed for **Mn-bpy^{diOMe}** relative to other Mn(I) complexes suggests a comparatively rapid hydride formation rate that meets or exceeds the rate of subsequent conversion to Mn–formate *via* CO_2 insertion (see bottom of Fig. S45). This, in turn, implies that **Mn-bpy^{diOMe}** sustains a higher steady-state concentration of the Mn–hydride species under photocatalytic conditions.

Theoretical calculations

From experimental investigations of the synthesized Mn(I) complexes, two distinct reactivity trends were identified in the photocatalytic reduction of CO_2, attributed to the presence of hydrogen bonding interactions involving Brønsted basic sites in the secondary coordination sphere. Specifically, (i) enhanced selectivity toward formate over CO and (ii) modulation of the Mn(I)–H formation rate, an essential step in formate generation, were observed. To rationalize the unique behavior of **Mn-bpy^{diOMe}**, the most efficient, selective formate-producing catalyst, we conducted DFT calculations. Geometry optimizations were performed using the unrestricted B3LYP functional with the def2-SVP basis set and the conductor-like polarizable continuum model (C-PCM; $\varepsilon = 37.22$ for DMF). Single-point energies were obtained at the B3LYP/def2-TZVPPD level of theory (see the Experimental section). The catalytic activation begins with the reduction of **Mn-bpy^{diOMe}** in the Mn(I) state to Mn(0) *via* electron transfer from $IrPS^{\bullet-}$, followed by cleavage of the Mn–Br bond. The first reduction, from Mn(I)–Br to $[Mn(I)–Br]^{1-}$, is calculated to occur at $E_{calc} = -2.44$ V *vs.* Fc^+/Fc, after which Br– is readily expelled to form Mn(0) with a Gibbs free energy change of $\Delta G = -12.62$ kcal mol^{-1}. The second reduction, generating the catalytically active intermediate $[Mn(0)L^{\bullet-}]^{1-}$, is computed to occur at $E_{calc} = -2.43$ V *vs.* Fc^+/Fc. Taken together, these steps correspond to an overall two-electron reduction occurring at $E_{calc} = -2.16$ V *vs.* Fc^+/Fc. The detailed procedure for calculating the reduction potentials of Mn complexes is described in SI Fig. S46–S48.[32,48] The analysis of the spin density and Mulliken spin population for $[Mn(0)L^{\bullet-}]^{1-}$ exhibits the antiferromagnetic configuration in which an unpaired electron at the Mn center is antiferromagnetically coupled with another unpaired electron residing in the π^* orbital of the bipyridine ligand (Fig. S49 and Tables S9–S11). Energy profiles were compared for pathways leading to both formate (Table S12) and CO (Table S13) as CO_2 reduction products.

The key step determining formate formation is the generation of the metal–hydride intermediate (blue line in Fig. 10 and 11), where the interaction between the proton donor and the catalytic site is critical. Under the catalytic conditions, TEOA reacts with oxidized $BIH^{\bullet+}$ to form TEOA(H), which is expected to deliver a proton to the Mn(0) center. A hydrogen bonding interaction between the terminal OH group of TEOA(H) and two ethylene-linked methoxy ($-(CH_2)_2$–OMe) groups stabilizes the intermediate, rendering this step exergonic ($\Delta G = -2.75$ kcal mol^{-1}) and facilitating Mn(I)–H formation *via* a low-energy transition state (TS-1a, $\Delta G^{\ddagger} = 1.61$ kcal mol^{-1}), yielding the

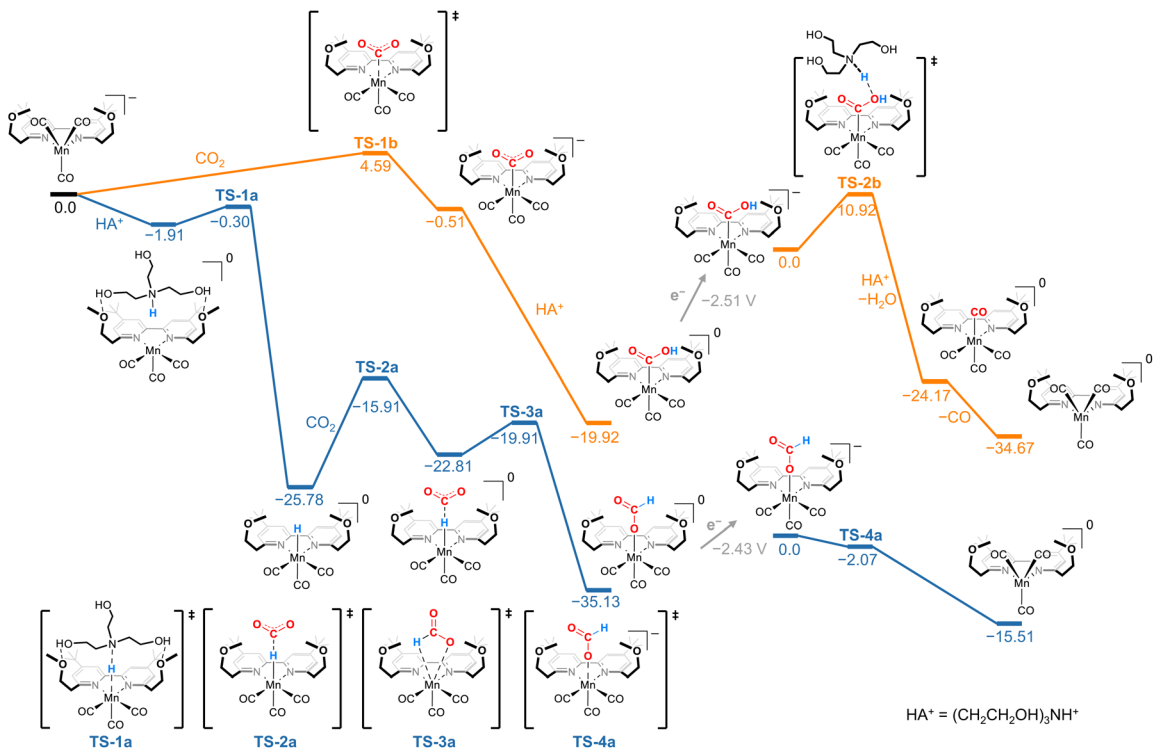

Fig. 10 Gibbs energy profiles (kcal mol^{-1}) for the competing CO_2 reduction pathways to formate (blue) and CO (orange) mediated by **Mn-bpy^{diOMe}**. The diagrams highlight the relative thermodynamic profiles and mechanistic divergence between the two product channels.

Mn(I)–H species ($\Delta G = -23.87$ kcal mol^{-1}). The subsequent reaction with the CO_2 molecule likely proceeds through an Mn(I)–H···CO_2 intermediate ($\Delta G = 2.97$ kcal mol^{-1}), leading to M^I-(η^1-OCHO) *via* TS-2a ($\Delta G^{\ddagger} = 9.88$ kcal mol^{-1}) and TS-3a ($\Delta G^{\ddagger} = 2.90$ kcal mol^{-1}), indicating a highly favorable pathway. The overall transformation from Mn(I)–H and CO_2 to M^I-(η^1-OCHO) is exergonic ($\Delta G = -9.35$ kcal mol^{-1}) and proceeds with a sufficiently low activation barrier. A further electron transfer leads to M^0-(η^1-OCHO) and facilitates the release of formate ($HCOO^-$) ($\Delta G = -15.51$ kcal mol^{-1}).

In the alternative pathway leading to CO formation (orange line in Fig. 10), direct reactivity of Mn(0) with CO_2 serves as the driving force. Formation of the Mn(I)–CO_2 intermediate is mildly exergonic ($\Delta G = -0.51$ kcal mol^{-1}), and the corresponding transition state (TS-1b) has a low barrier ($\Delta G^{\ddagger} = 4.59$ kcal mol^{-1}), supporting its feasibility. In the presence of TEOA(H), the formation of M^I-(η^1-C(O)OH) is energetically favorable ($\Delta G = -19.41$ kcal mol^{-1}). Subsequent electron transfer gives M^0-(η^1-C(O)OH), which undergoes protonation to cleave the C(O)–OH bond, releasing a H_2O molecule. The formation of Mn^0–CO is exergonic ($\Delta G = -24.17$ kcal mol^{-1}), with the transition state (TS-2b) calculated at $\Delta G^{\ddagger} = 10.92$ kcal mol^{-1}. Finally, CO is released from the Mn(0) center ($\Delta G = -10.50$ kcal mol^{-1}), completing the catalytic cycle. Overall, both formate and CO formation pathways from CO_2 reduction are thermodynamically accessible. However, the hydrogen bonding interaction between two –$(CH_2)_2$–OMe groups and TEOA(H) significantly lowers the activation energy for Mn(I)–H formation, thereby enhancing selectivity for formate over CO. Also, we examined the H_2 evolution pathway from Mn(I)–H. Formation of the Mn(I)–H_2 intermediate is endergonic, with a ΔG of 10.19 kcal mol^{-1} (Fig. S50), which is consistent with the experimentally observed selectivity toward formate formation.

To assess the generality of this hydrogen bonding effect, the catalytic process of **Mn-bpy^{OMe}** was investigated as a comparative system. Theoretical studies on **Mn-bpy^{OMe}** corroborate the experimental findings; energy profiles for the formate and CO pathways are shown in Fig. 11 (see Tables S14 and S15). Like **Mn-bpy^{diOMe}**, the metal center of **Mn-bpy^{OMe}** is reduced to Mn(0) by $IrPS^{\bullet-}$, followed by cleavage of the Mn–Br bond for catalyst activation. Although a singlet Mn(0) species forms an intermediate *via* a single hydrogen bond between one –$(CH_2)_2$–OMe group and TEOA(H) ($\Delta G = -0.09$ kcal mol^{-1}), this stabilization is weaker than in **Mn-bpy^{diOMe}**. Mn(I)–H formation remains exergonic ($\Delta G = -22.77$ kcal mol^{-1}), but the transition state (TS-1a′, $\Delta G^{\ddagger} = 2.60$ kcal mol^{-1}) is slightly higher in energy relative to that of **Mn-bpy^{diOMe}**. Although formate remains the predominant product, the diminished formate/CO ratio observed for **Mn-bpy^{OMe}** likely arises from less effective stabilization of the protonation intermediate relative to **Mn-bpy^{diOMe}**. Furthermore, the activation barrier and Gibbs free energy change for Mn(I)–H formation were computed for the unfunctionalized **Mn-bpy** catalyst (Fig. S51). **Mn-bpy** exhibits a less favorable Gibbs free energy change for Mn–hydride formation ($\Delta G = -20.69$ kcal mol^{-1}) compared to **Mn-bpy^{diOMe}** ($\Delta G = -23.87$ kcal mol^{-1}), along with a higher activation barrier ($\Delta G^{\ddagger} = 3.43$ kcal mol^{-1} *vs.* 1.61 kcal mol^{-1} for **Mn-bpy^{diOMe}**, TS-1a). Kinetic measurements of metal–hydride formation (Fig. 9)

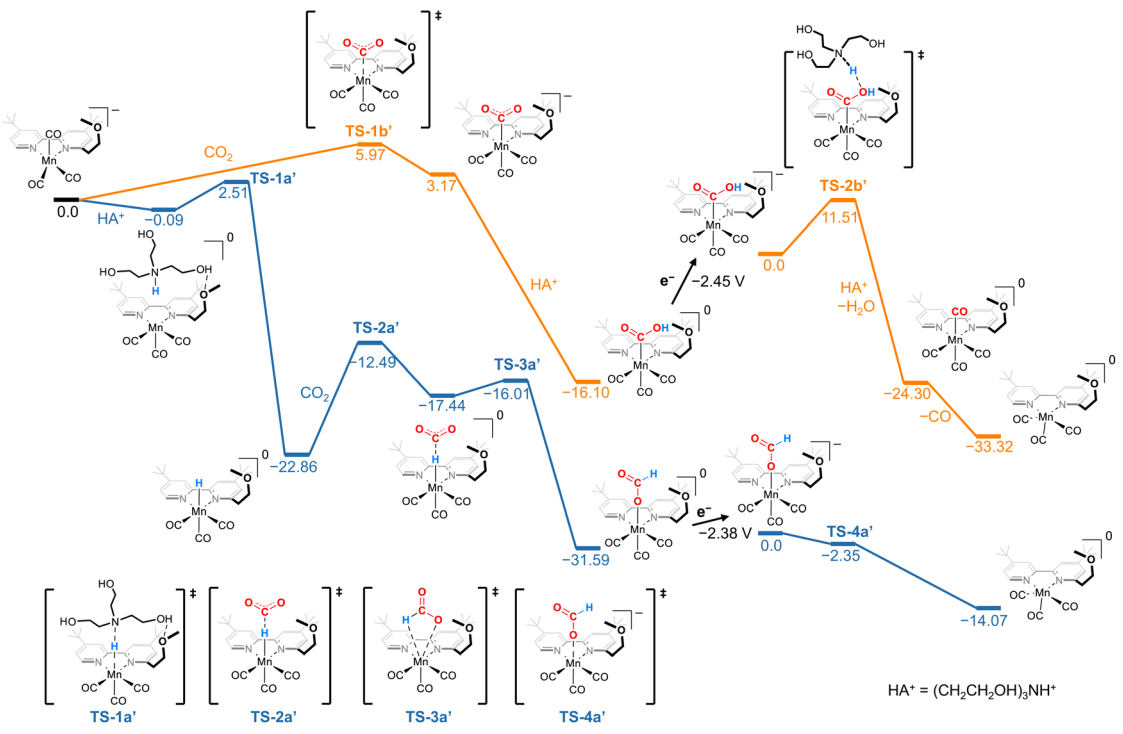

Fig. 11 Gibbs energy profiles (kcal mol^{-1}) for the competing CO_2 reduction pathways to formate (blue) and CO (orange) mediated by **Mn-bpy^{OMe}**. The diagrams highlight the relative thermodynamic profiles and mechanistic divergence between the two product channels.

reveal an accelerated Mn(I)–H formation rate for **Mn-bpy^{diOMe}**, in agreement with the computed reaction profiles. The energy span model proposed by Kozuch and co-workers was employed to evaluate the product selectivity between the CO and formate formation pathways (Fig. S52 and S53).[49,50] For the CO formation pathway, the energy span (δE) was calculated to be 10.92 kcal mol^{-1}, corresponding to a calculated turnover frequency (TOF) of 6×10^4 s^{-1}. In contrast, for the formate formation pathway, δE was calculated to be 2.07 kcal mol^{-1}, yielding a TOF of 2×10^{11} s^{-1}. Based on these TOF values, the fractional turnover frequencies were determined to be $X_{TOF,CO} = 3 \times 10^{-7}$ and $X_{TOF,formate} = 0.999$, indicating a selectivity toward formate formation. Taken together, these results underscore the pivotal role of second-sphere hydrogen-bonding interactions in stabilizing key catalytic intermediates and steering the reaction pathway toward selective formate generation during CO_2 photoreduction. This mechanistic feature is consistent with the pronounced dependence on TEOA concentration observed in the photolysis experiments (Table 2 and Fig. S28–S31), further supporting the notion that intermolecular proton relays are central to enabling efficient CO_2-to-formate conversion.

Discussion

In the monomeric two-electron CO_2 reduction using an organometallic mono-bipyridyl Mn(I) complex, where the uncontrolled Mn–Mn dimeric pathway is avoided, product selectivity (formate *vs.* CO) primarily depends on the competition between Mn–hydride and Mn(η^1-C(O)OH) intermediates during catalysis.[23,36] Specifically, after the (L)Mn(CO)$_3$Br catalyst undergoes a two-electron reduction, CO_2 molecules bind to the Mn center of the resulting two electron-reduced [(L)Mn^0(CO)$_3$]$^-$ species. If a proton is introduced at this stage, (L)Mn(CO)$_3$(η^1-C(O)OH) forms as a key intermediate for CO generation. Conversely, if the [(L)Mn^0(CO)$_3$]$^-$ species receives a proton before CO_2 binding, Mn–hydride species, (L)Mn(CO)$_3$H, are predominantly formed, serving as intermediates for formate production. Under uncontrolled conditions, however, Mn–Mn dimerization has been reported to promote CO formation during catalysis.[10,51] Therefore, promoting Mn–hydride formation while inhibiting Mn–Mn dimerization is essential for enhancing the efficiency and selectivity of CO_2-to-formate conversion in Mn(I)-based photocatalytic systems.

Based on the photolysis experiments, *operando* FTIR analysis, and theoretical calculation, the CO_2 reduction mechanism of the SCL-substituted Mn(I) catalyst can be expressed as shown in Fig. 12 and 13. As investigated in the above *in situ* FTIR spectro-photochemical study, the SCL-functionalized Mn(I) complexes follow a monomeric pathway rather than dimerization due to steric hindrance of the bulky SCL suppressing intermolecular interaction. The Mn(I) catalyst undergoes a two-electron reduction by the reductively quenched Ir(III) photosensitizer (IrPS$^{\bullet -}$) to generate [(L)Mn^0(CO)$_3$]$^-$. At this stage, the substituted SCL facilitates proton transfer, leading to the formation of the Mn–hydride intermediate. As a representative example, the theoretical calculation demonstrated that two alkoxy groups of **Mn-bpy^{diOMe}** can help form a hydrogen bond between TEOA(H) and the Mn(I) complex, positioning the proton bound to the nitrogen of TEOA(H) closer to the Mn metal center, thereby promoting Mn–hydride intermediate formation (step b and c in Fig. 12). The movie in the SI illustrates the effective proton-shuttling process mediated by intermolecular O–H···O hydrogen bonding between the two alkoxy secondary coordination sphere ligands of **Mn-bpy^{diOMe}** and the OH groups of TEOA(H), ultimately facilitating formate generation from the resulting Mn–H intermediate. The snapshot taken from the SI movie (right panel of Fig. 12) represents the computed structure

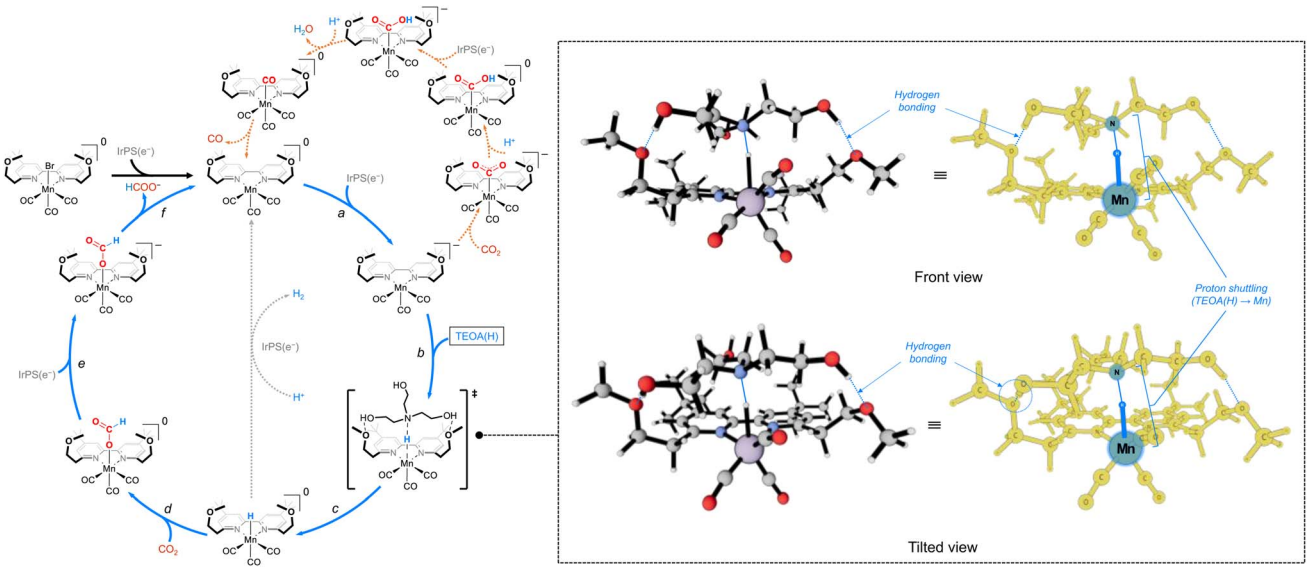

Fig. 12 Proposed catalytic cycle for photocatalytic CO_2-to-formate/CO conversion mediated by **Mn-bpy^{diOMe}** in the mixed homogeneous system. The right panel displays a snapshot from the SI movie, corresponding to the calculated structure captured during the proton-shuttling step, in which TEOA(H) transfers a proton to the reduced Mn center *via* an intermolecular hydrogen-bonding network.

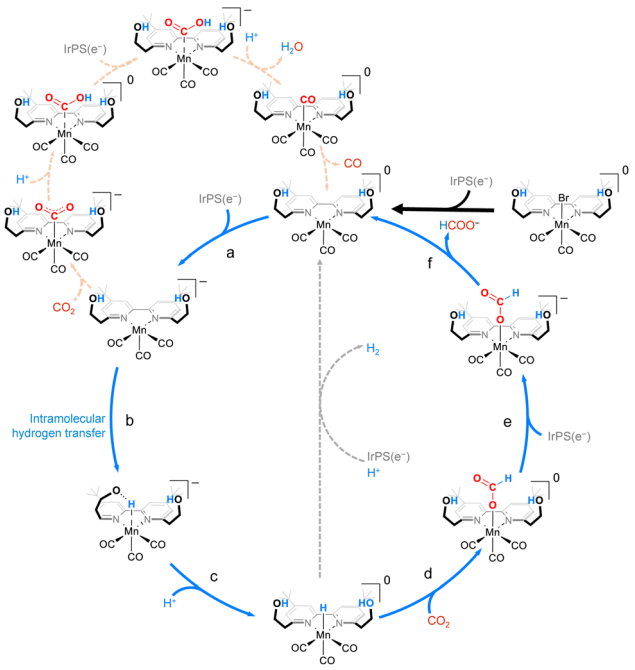

Fig. 13 Proposed catalytic cycle of the photocatalytic CO_2-to-formate/CO conversion mediated by **Mn-bpy^{diOH}** in the mixed homogeneous system.

at the proton-shuttling step, wherein TEOA(H) delivers a proton to the reduced Mn center through an intermolecular hydrogen-bonding network. Meanwhile, the –OH group is expected to facilitate direct intramolecular hydrogen transfer to the adjacent Mn metal center faster than proton transfer from TEOA(H), as reported in previous studies on Ru(II) catalysts where the OH-tethered ligand acted as a Brønsted acid, delivering protons to the nearby Ru center (step b in the cycle in Fig. 13).[47] This is because the pK_a of –OH (13.20)[52] is lower than that of TEOA(H) (15.9 in ACN).[53] This plausible mechanism is supported by the above *operando* FTIR experimental results, where **Mn-bpy^{OH}** and **Mn-bpy^{diOH}** catalysts exhibited relatively faster Mn–hydride formation compared to **Mn-bpy^{OMe}** and **Mn-bpy^{diOMe}** catalysts (Fig. 8). However, despite the faster formation of Mn–hydride intermediates in Mn catalysts with –OH groups compared to those with alkoxy groups, the overall photolysis results show that catalysts with alkoxy groups produce a higher amount of formate. This discrepancy can be attributed to an additional step required in **Mn-bpy^{OH}** and **Mn-bpy^{diOH}** with –OH groups: after intramolecular hydrogen transfer ($-(CH_2)_2-OH$ + Mn → $-(CH_2)_2-O^-$ + Mn–H), the resulting $-(CH_2)_2-O^-$ pendant must receive a proton from TEOA(H), introducing an inefficiency in the overall CO_2 reduction catalytic cycle (step c in the cycle in Fig. 13). In the next step, as widely reported in related studies,[4,5,7,10–12] CO_2 is inserted into the Mn–hydride intermediate, forming Mn–formate ((L)Mn(η^1-OCHO)(CO)$_3$), which undergoes further reduction by IrPS$^{\bullet-}$ before releasing formate (steps d, e, and f in Fig. 12 and 13).

Regarding the catalytic pathway following the formation of the Mn–hydride intermediate, it has been reported that in electrochemical CO_2 reduction using a mono-bipyridyl Mn(I) catalyst, the pathway is highly dependent on the applied overpotential.[10,23] Under high overpotential (HO) conditions of approximately −2.02 V *vs.* Fc^+/Fc or more, the "reduction-first pathway" operates, in which the Mn–hydride intermediate undergoes a one-electron reduction before CO_2 insertion.[54] Conversely, under low overpotential (LO) conditions of approximately −1.70 V *vs.* Fc^+/Fc or more, it has been proposed that CO_2 is first inserted into the Mn–H bond before electron transfer occurs, favoring the "CO_2 insertion-first pathway".[23,32,36] In this context, the current photochemical CO_2 reduction system, in which electrons are gradually supplied to the Mn(I) catalyst *via* reductively quenched IrPS (E_{red} = −1.78 V *vs.* Fc^+/Fc), is expected to follow the low-overpotential CO_2 insertion-first pathway (Fig. S54).[7,36] This behavior contrasts with electrochemical CO_2 reduction, which is highly sensitive to the applied overpotential.

Conclusions

The influence of secondary coordination on the mono-bipyridyl Mn(I) complex, [(L)Mn(CO)$_3$Br], was investigated by incorporating saturated ethylene ($-(CH_2)_2-$)-bridged Brønsted acidic/basic secondary coordination ligands (SCLs): ethylene hydroxy ($-(CH_2)_2-OH$) and ethylene alkoxy ($-(CH_2)_2-OMe/OEt$). The mechanistic study investigating the efficiency of metal–hydride formation through electrochemical and *operando* FTIR spectrochemical analysis showed that (1) the steric hindrance of the secondary coordination ligand (SCL) effectively prevents the Mn–Mn dimerization pathway of the reduced Mn(I) catalyst, which otherwise decreases the product selectivity and activity for CO_2 reduction, and (2) the introduction of the SCL promotes the formation rate of the Mn–hydride intermediate and enhances CO_2-to-formate conversion activity *via* the Mn–H intermediate. As a representative example, **Mn-bpy^{diOMe}** possessing two ethylene methoxy groups ($-(CH_2)_2-OMe$) exhibited the highest CO_2-to-formate conversion activity, achieving 94% formate selectivity. Theoretical calculation and experimental data (CVs and *in situ* FTIR) demonstrated that two alkoxy groups facilitate hydrogen bonding between TEOA(H) and the Mn(I) complex. This interaction positions the proton bound to the nitrogen of TEOA(H) closer to the Mn metal center, thereby enhancing Mn–hydride intermediate formation. Overall, this study highlights the role of the SCL as an internal proton relay that directs protons toward the nucleophilic metal center, thereby governing the kinetics of two competing post-reduction pathways (M–COOH *vs.* M–H). The type and number of SCL units significantly influence the catalytic activity and selectivity in CO_2-to-formate/CO conversion.

Author contributions

H.-J. Son designed the project and directed the work. M.-J. Bong and D. Lee performed all synthetic experiments, and W. Lee performed all DFT calculations. M.-J. Bong, W. Lee, H. Kim, J. Seo, and H.-J. Son wrote the paper. All authors discussed, read and commented on the manuscript.

Conflicts of interest

There are no conflicts to declare.

Data availability

CCDC 2500002 (**Mn-bpy^{diOMe}**) and 2500003 (**Mn-bpy^{OEt}**) contain the supplementary crystallographic data for this paper.[55a,b]

All supporting data are provided within the article and its supplementary information (SI). Supplementary information: experimental procedures, X-ray crystallographic data, ^{1}H NMR and ESI-MS spectra, plots of CO and formate formation *versus* time, GC-MS data, cyclic voltammograms, *operando* FTIR spectra, and theoretical calculations. See DOI: https://doi.org/10.1039/d5sc09412g.

Acknowledgements

This work was supported by the Basic Science Research Program through the National Research Foundation of Korea (NRF) grant funded by the Korea government (MSIT) (RS-2025-00562897 and RS-2021-NR060081) and by a Korea University Grant.

Notes and references

1 International Energy Agency Global Energy Review 2025: CO_2 Emissions, accessed December 2025.
2 N. Mac Dowell, P. S. Fennell, N. Shah and G. C. Maitland, The role of CO_2 capture and utilization in mitigating climate change, *Nat. Clim. Change*, 2017, **7**, 243–249, DOI: 10.1038/nclimate3231.
3 M. E. Boot-Handford, J. C. Abanades, E. J. Anthony, M. J. Blunt, S. Brandani, N. Mac Dowell, J. R. Fernández, M.-C. Ferrari, R. Gross, J. P. Hallett, R. S. Haszeldine, P. Heptonstall, A. Lyngfelt, Z. Makuch, E. Mangano, R. T. J. Porter, M. Pourkashanian, G. T. Rochelle, N. Shah, J. G. Yao and P. S. Fennell, Carbon capture and storage update, *Energy Environ. Sci.*, 2014, **7**, 130–189, DOI: 10.1039/C3EE42350F.
4 N. Elgrishi, M. B. Chambers, X. Wang and M. Fontecave, Molecular Polypyridine-based Metal Complexes as Catalysts for the Reduction of CO_2, *Chem. Soc. Rev.*, 2017, **46**, 761–796, DOI: 10.1039/C6CS00391A.
5 C. D. Windle and R. N. Perutz, Advances in Molecular Photocatalytic and Electrocatalytic CO_2 Reduction, *Coord. Chem. Rev.*, 2012, **256**, 2562–2570, DOI: 10.1016/j.ccr.2012.03.010.
6 H. Takeda, C. Cometto, O. Ishitani and M. Robert, Electrons, Photons, Protons and Earth-Abundant Metal Complexes for Molecular Catalysis of CO_2 Reduction, *ACS Catal.*, 2017, **7**, 70–88, DOI: 10.1021/acscatal.6b02181.
7 Y. Yamazaki, H. Takeda and O. Ishitani, Photocatalytic Reduction of CO_2 using Metal Complexes, *J. Photochem. Photobiol., C*, 2015, **25**, 106–137, DOI: 10.1016/j.jphotochemrev.2015.09.001.
8 C. Costentin, M. Robert and J.-M. Savéant, Catalysis of the Electrochemical Reduction of Carbon Dioxide, *Chem. Soc. Rev.*, 2013, **42**, 2423–2436, DOI: 10.1039/C2CS35360A.
9 J. Qiao, Y. Liu, F. Hong and J. Zhang, A Review of Catalysts for the Electroreduction of Carbon Dioxide to Produce Low-Carbon Fuels, *Chem. Soc. Rev.*, 2014, **43**, 631–675, DOI: 10.1039/C3CS60323G.
10 D. C. Grills, M. Z. Ertem, K. T. Ngo and J. Rochford, Mechanistic Aspects of CO_2 Reduction Catalysis with Manganese-Based Molecular Catalysts, *Coord. Chem. Rev.*, 2018, **374**, 173–217, DOI: 10.1016/j.ccr.2018.05.002.
11 Y. Kuramochi, O. Ishitani and H. Ishida, Reaction Mechanisms of Catalytic Photochemical CO_2 Reduction Using Re(I) and Ru(II) Complexes, *Coord. Chem. Rev.*, 2018, **373**, 333–356, DOI: 10.1016/j.ccr.2017.11.023.
12 K. E. Dalle, J. Warnan, J. J. Leung, B. Reuillard, I. S. Karmel and E. Reisner, Electro- and Solar-Driven Fuel Synthesis with First Row Transition Metal Complexes, *Chem. Rev.*, 2019, **119**, 2752–2875, DOI: 10.1021/acs.chemrev.8b00293.
13 J. W. Peters, W. N. Lanzilotta, B. J. Lemon and L. C. Seefeldt, X-ray Crystal Structure of the Fe-Only Hydrogenase (CpI) from Clostridium pasteurianum to 1.8 Angstrom Resolution, *Science*, 1998, **282**, 1853–1858, DOI: 10.1126/science.282.5395.1853.
14 P. M. Vignais, B. Billoud and J. Meyer, Classification and phylogeny of hydrogenases, *FEMS Microbiol. Rev.*, 2001, **25**, 455–501, DOI: 10.1111/j.1574-6976.2001.tb00587.x.
15 D. Schilter, J. M. Camara, M. T. Huynh, S. Hammes-Schiffer and T. B. Rauchfuss, Hydrogenase Enzymes and Their Synthetic Models: The Role of Metal Hydrides, *Chem. Rev.*, 2016, **116**, 8693–8749, DOI: 10.1021/acs.chemrev.6b00180.
16 M. Haake, B. Reuillard, M. Chavarot-Kerlidou, C. Costentin and V. Artero, Proton Relays in Molecular Catalysis for Hydrogen Evolution and Oxidation: Lessons From the Mimicry of Hydrogenases and Electrochemical Kinetic Analyses, *Angew. Chem., Int. Ed.*, 2024, **63**, e202413910, DOI: 10.1002/anie.202413910.
17 A. Adamska, A. Silakov, C. Lambertz, O. Rüdiger, T. Happe, E. Reijerse and W. Lubitz, Identification and characterization of the "superreduced" state of the H-cluster in [FeFe] hydrogenase: a new building block for the catalytic cycle?, *Angew. Chem., Int. Ed.*, 2012, **51**, 11458–11462, DOI: 10.1002/anie.201204800.
18 P. Trogadas, L. Xu and M.-O. Coppens, From Biomimicking to Bioinspired Design of Electrocatalysts for CO_2 Reduction to C_1 Products, *Angew. Chem., Int. Ed.*, 2024, **63**, e202314446, DOI: 10.1002/anie.202314446.
19 M. W. Drover, A Guide to Secondary Coordination Sphere Editing, *Chem. Soc. Rev.*, 2022, **51**, 1861–1880, DOI: 10.1039/D2CS00022A.
20 C. S. Durfy, J. A. Zurakowski and M. W. Drover, A Blueprint for Secondary Coordination Sphere Editing: Approaches Toward Lewis-Acid Assisted Carbon Dioxide Co-Activation, *ChemSusChem*, 2024, **17**, e202400039, DOI: 10.1002/cssc.202400039.

21 A. W. Nichols and C. W. Machan, Secondary-Sphere Effects in Molecular Electrocatalytic CO_2 Reduction, *Front. Chem.*, 2019, **7**, 397, DOI: 10.3389/fchem.2019.00397.

22 C. Costentin, S. Drouet, M. Robert and J. M. Savéant, A Local Proton Source Enhances CO_2 Electroreduction to CO by a Molecular Fe Catalyst, *Science*, 2012, **338**, 90–94, DOI: 10.1126/science.1224581.

23 M. H. Rønne, D. Cho, M. R. Madsen, J. B. Jakobsen, S. Eom, É. Escoudé, H. C. D. Hammershøj, D. U. Nielsen, S. U. Pedersen, M.-H. Baik, T. Skrydstrup and K. Daasbjerg, Ligand-Controlled Product Selectivity in Electrochemical Carbon Dioxide Reduction Using Manganese Bipyridine Catalysts, *J. Am. Chem. Soc.*, 2020, **142**, 4265–4275, DOI: 10.1021/jacs.9b11806.

24 E. M. Nichols, J. S. Derrick, S. K. Nistanaki, P. T. Smith and C. J. Chang, Positional Effects of Second-Sphere Amide Pendants on Electrochemical CO_2 reduction Catalyzed by Iron Porphyrins, *Chem. Sci.*, 2018, **9**, 2952–2960, DOI: 10.1039/C7SC04682K.

25 A. Chapovetsky, T. H. Do, R. Haiges, M. K. Takase and S. C. Marinescu, Proton-Assisted Reduction of CO_2 by Cobalt Aminopyridine Macrocycles, *J. Am. Chem. Soc.*, 2016, **138**, 5765–5768, DOI: 10.1021/jacs.6b01980.

26 S. Roy, B. Sharma, J. Pecaut, P. Simon, M. Fontecave, P. D. Tran, E. Derat and V. Artero, Molecular Cobalt Complexes with Pendant Amines for Selective Electrocatalytic Reduction of Carbon Dioxide to Formic Acid, *J. Am. Chem. Soc.*, 2017, **139**, 3685–3696, DOI: 10.1021/jacs.6b11474.

27 A. Chapovetsky, M. Welborn, J. M. Luna, R. Haiges, T. F. Miller III and S. C. Marinescu, Pendant Hydrogen-Bond Donors in Cobalt Catalysts Independently Enhance CO_2 Reduction, *ACS Cent. Sci.*, 2018, **4**, 397–404, DOI: 10.1021/acscentsci.7b00607.

28 A. D. Wilson, R. K. Shoemaker, A. Meidaner, J. T. Muckerman, D. L. DuBois and M. Rakowski DuBois, Nature of Hydrogen Interactions with Ni(II) Complexes Containing Cyclic Phosphine Ligands with Pendant Nitrogen Bases, *Proc. Natl. Acad. Sci. U. S. A.*, 2007, **104**, 6951–6956, DOI: 10.1073/pnas.0608928104.

29 M. Rakowski DuBois and D. L. DuBois, Development of Molecular Electrocatalysts for CO_2 Reduction and H_2 Production/Oxidation, *Acc. Chem. Res.*, 2009, **42**, 1974–1982, DOI: 10.1021/ar900110c.

30 C. L. Montgomery, J. Amtawong, A. M. Jordan, D. A. Kurtz and J. L. Dempsey, Proton transfer kinetics of transition metal hydride complexes and implications for fuel-forming reactions, *Chem. Soc. Rev.*, 2023, **52**, 7137–7169, DOI: 10.1039/D3CS00355H.

31 F. Hartl, P. Rosa, L. Ricard, P. L. Floch and S. Zalis, Electronic Transitions and Bonding Properties in a Series of Five-Coordinate "16-Electron" Complexes $[Mn(CO)_3(L_2)]^-$ (L_2= Chelating Redox-Active π-Donor Ligand), *Coord. Chem. Rev.*, 2007, **251**, 557–576, DOI: 10.1016/j.ccr.2006.09.003.

32 W. Hong, M. Luthra, J. B. Jakobsen, M. R. Madsen, A. C. Castro, H. C. D. Hammershøj, S. U. Pedersen, D. Balcells, T. Skrydstrup, K. Daasbjerg and A. Nova, Exploring the Parameters Controlling Product Selectivity in Electrochemical CO_2 Reduction in Competition with Hydrogen Evolution Employing Manganese Bipyridine Complexes, *ACS Catal.*, 2023, **13**, 3109–3119, DOI: 10.1021/acscatal.2c05951.

33 F. Franco, C. Cometto, L. Nencini, C. Barolo, F. Sordello, C. Minero, J. Fiedler, M. Robert, R. Gobetto and C. Nervi, Local Proton Source in Electrocatalytic CO_2 Reduction with $[Mn(bpy\text{-}R)(CO)_3Br]$ Complexes, *Chem.–Eur. J.*, 2017, **23**, 4782–4793, DOI: 10.1002/chem.201605546.

34 K. T. Ngo, M. McKinnon, B. Mahanti, R. Narayanan, D. C. Grills, M. Z. Ertem and J. Rochford, Turning on the Protonation-First Pathway for Electrocatalytic CO_2 Reduction by Manganese Bipyridyl Tricarbonyl Complexes, *J. Am. Chem. Soc.*, 2017, **139**, 2604–2618, DOI: 10.1021/jacs.6b08776.

35 F. Franco, C. Cometto, F. F. Vallana, F. Sordello, E. Priola, C. Minero, C. Nervi and R. Gobetto, A Local Proton Source in a $[Mn(bpy\text{-}R)(CO)_3Br]$-Type Redox Catalyst Enables CO_2 Reduction Even in the Absence of Brønsted Acids, *Chem. Commun.*, 2014, **50**, 14670–14673, DOI: 10.1039/C4CC05563B.

36 S. S. Roy, K. Talukdar and J. W. Jurss, Electro- and Photochemical Reduction of CO_2 by Molecular Manganese Catalysts: Exploring the Positional Effect of Second-Sphere Hydrogen-Bond Donors, *ChemSusChem*, 2021, **14**, 662–670, DOI: 10.1002/cssc.202002648.

37 J. Agarwal, T. W. Shaw, H. F. Schaefer III and A. B. Bocarsly, Design of a Catalytic Active Site for Electrochemical CO_2 Reduction with Mn(I)-Tricarbonyl Species, *Inorg. Chem.*, 2015, **54**, 5285–5294, DOI: 10.1021/acs.inorgchem.5b00233.

38 M. R. Madsen, M. H. Rønne, M. Heuschen, D. Golo, M. S. G. Ahlquist, T. Skrydstrup, S. U. Pedersen and K. Daasbjerg, Promoting Selective Generation of Formic Acid from CO_2 Using $Mn(bpy)(CO)_3Br$ as Electrocatalyst and Triethylamine/Isopropanol as Additives, *J. Am. Chem. Soc.*, 2021, **143**, 20491–20500, DOI: 10.1021/jacs.1c10805.

39 S. J. Liu, Q. Zhao, Q. L. Fan and W. Huang, A Series of Red-Light-Emitting Ionic Iridium Complexes: Structures, Excited State Properties, and Application in Electroluminescent Devices, *Eur. J. Inorg. Chem.*, 2008, **2008**, 2177–2185, DOI: 10.1002/ejic.200701184.

40 M. Gaydou, T. Moragas, F. Juliá-Hernández and R. Martin, Site-Selective Catalytic Carboxylation of Unsaturated Hydrocarbons with CO_2 and Water, *J. Am. Chem. Soc.*, 2017, **139**, 12161–12164, DOI: 10.1021/jacs.7b07637.

41 S.-Z. Sun, C. Romano and R. Martin, Site-Selective Catalytic Deaminative Alkylation of Unactivated Olefins, *J. Am. Chem. Soc.*, 2019, **141**, 16197–16201, DOI: 10.1021/jacs.9b07489.

42 H. Takeda, H. Kamiyama, K. Okamoto, M. Irimajiri, T. Mizutani, K. Koike, A. Sekine and O. Ishitani, Highly Efficient and Robust Photocatalytic Systems for CO_2 Reduction Consisting of a Cu(I) Photosensitizer and Mn(I) catalysts, *J. Am. Chem. Soc.*, 2018, **140**, 17241–17254, DOI: 10.1021/jacs.8b10619.

43 Y. Kuramochi, J. Itabashi, K. Fukaya, A. Enomoto, M. Yoshida and H. Ishida, Unexpected Effect of Catalyst Concentration on Photochemical CO_2 Reduction by *trans*(Cl)-Ru(bpy)$(CO)_2Cl_2$: New Mechanistic Insight into the CO/$HCOO^-$ Selectivity, *Chem. Sci.*, 2015, **6**, 3063–3074, DOI: 10.1039/C5SC00199D.

44 M. D. Sampson, A. D. Nguyen, K. A. Grice, C. E. Moore, A. L. Rheingold and C. P. Kubiak, Manganese Catalysts with Bulky Bipyridine Ligands for the Electrocatalytic Reduction of Carbon Dioxide: Eliminating Dimerization and Altering Catalysis, *J. Am. Chem. Soc.*, 2014, **136**, 5460–5471, DOI: 10.1021/ja501252f.

45 D. C. Grills, J. A. Farrington, B. H. Layne, S. V. Lymar, B. A. Mello, J. M. Preses and J. F. Wishart, Mechanism of the Formation of a Mn-Based CO_2 Reduction Catalyst Revealed by Pulse Radiolysis with Time-Resolved Infrared Detection, *J. Am. Chem. Soc.*, 2014, **136**, 5563–5566, DOI: 10.1021/ja501051s.

46 M. D. Sampson and C. P. Kubiak, Manganese Electrocatalysts with Bulky Bipyridine Ligands: Utilizing Lewis Acids to Promote Carbon Dioxide Reduction at Low Overpotentials, *J. Am. Chem. Soc.*, 2016, **138**, 1386–1393, DOI: 10.1021/jacs.5b12215.

47 C. Back, Y. Seo, S. Choi, M. S. Choe, D. Lee, J.-O. Baeg, H.-J. Son and S. O. Kang, Secondary Coordination Effect on Monobipyridyl Ru(II) Catalysts in Photochemical CO_2 Reduction: Effective Proton Shuttle of Pendant Brønsted Acid/Base Sites (OH and $N(CH_3)_2$) and Its Mechanistic Investigation, *Inorg. Chem.*, 2021, **60**, 14151–14164, DOI: 10.1021/acs.inorgchem.1c01559.

48 M. Luthra, A. C. Castro, D. Balcells, K. Daasbjerg and A. Nova, Metal-dependent mechanism of the electrocatalytic reduction of CO_2 by bipyridine complexes bearing pendant amines: a DFT study, *ACS Org. Inorg. Au*, 2024, **5**, 26–36, DOI: 10.1021/acsorginorgau.4c00046.

49 X. Li and J. A. Panetier, Computational Study on the Reactivity of Imidazolium-Functionalized Manganese Bipyridyl Tricarbonyl Electrocatalysts [Mn[bpyMe(Im-R)$_3$Br]$^+$ (R = Me, Me_2 and Me_4) for CO_2-to-CO Conversion Over H_2 Formation, *Phys. Chem. Chem. Phys.*, 2021, **23**, 14940–14951, DOI: 10.1039/D1CP01576A.

50 S. Kozuch and S. Shaik, How to Conceptualize Catalytic Cycles? The Energetic Span Model, *Acc. Chem. Res.*, 2011, **44**, 101–110, DOI: 10.1021/ar1000956.

51 S.-J. Woo, S. Choi, S.-Y. Kim, P. S. Kim, J. H. Jo, C. H. Kim, H.-J. Son, C. Pac and S. O. Kang, Highly Selective and Durable Photochemical CO_2 Reduction by Molecular Mn(I) Catalyst Fixed on a Particular Dye-Sensitized TiO_2 Platform, *ACS Catal.*, 2019, **9**, 2580–2593, DOI: 10.1021/acscatal.8b03816.

52 E. Rossini, A. D. Bochevarov and E. W. Knapp, Empirical Conversion of pK_a Values between Different Solvents and Interpretation of the Parameters: Application to Water, Acetonitrile, Dimethyl Sulfoxide, and Methanol, *ACS Omega*, 2018, **3**, 1653–1662, DOI: 10.1021/acsomega.7b01895.

53 R. N. Sampaio, D. C. Grills, D. E. Polyansky, D. J. Szalda and E. Fujita, Unexpected roles of Triethanolamine in the Photochemical Reduction of CO_2 to Formate by Ruthenium Complexes, *J. Am. Chem. Soc.*, 2020, **142**, 2413–2428, DOI: 10.1021/jacs.9b11897.

54 S. Sung, X. Li, L. M. Wolf, J. R. Meeder, N. S. Bhuvanesh, K. A. Grice, J. A. Panetier and M. Nippe, Synergistic Effects of Imidazolium-Functionalization on *fac*-Mn$(CO)_3$ Bipyridine Catalyst Platforms for Electrocatalytic Carbon Dioxide Reduction, *J. Am. Chem. Soc.*, 2019, **141**, 6569–6582, DOI: 10.1021/jacs.8b13657.

55 (*a*) CCDC 2500002: Experimental Crystal Structure Determination, 2026, DOI: 10.5517/ccdc.csd.cc2pxg7b; (*b*) CCDC 2500003: Experimental Crystal Structure Determination, 2026, DOI: 10.5517/ccdc.csd.cc2pxg8c.